Assessing the plausibility of direct constraints on ancient atmospheric pCO₂ from fluid inclusions in halite: A theoretical and experimental approach

Michael Naylor Hudgins[1,2], Justin G. Park[1,2], Alex M. Ryan[1,2], Jessika A. Rogers[3], and Morgan F. Schaller[1,2]*

[1]Department of Earth and Environmental Sciences, Rensselaer Polytechnic Institute, Troy, NY, USA.

[2]Center for Environmental and Stable Isotope Analysis, Rensselaer Polytechnic Institute, Troy, NY, USA.

[3]Department of Physics, Applied Physics, and Astronomy, Rensselaer Polytechnic Institute, Troy, NY, USA.

Abstract

Fluid inclusions in halite formed in surficial environments have recently gained attention for their ability to capture and preserve samples of ancient air, and by mechanical decrepitation, these inclusion gases can be quantified via mass spectrometry. However, it has yet to be demonstrated that the CO_2 content measured on halite accurately represents the overlying air at various CO_2 concentrations and not the exsolution of some or all of the dissolved inorganic carbon. Based on the kinetics of the carbonate system equilibrium and aqueous solubility of CO_2, we hypothesize that the CO_2 measured by bulk analysis of fluid inclusion gas is derived solely from a mixture between $CO_{2\,(g)}$ and $[CO_2]_{aq}$ (CO_2 from air and air-saturated brine). To address this, we first conducted depressurization experiments on atmospherically equilibrated carbonate solutions, and by mass balance we show that only $CO_{2(aq)}$ degasses during solution depressurization, while the remaining HCO_3^- and CO_3^{2-} combine with Na^+ cations to precipitate $NaHCO_3$ salt. In addition, we performed mechanical decrepitation experiments on lab-grown halite that was precipitated in a sealed pressure vessel under various pCO₂ conditions (450 ppm, 3000 ppm, and 5000 ppm). Volatile contents of the carbonate solutions and the lab-grown halite were analyzed with a quadrupole mass spectrometer. Measured CO_2 content falls between the expected values of air and air-saturated brine for the different pCO₂ conditions, and by partitioning the gas contributions from each phase, we observe atmospheric pCO₂ that closely matches the starting conditions. Our findings demonstrate that inclusions in halite faithfully entrap and preserve CO_2 from the overlying atmosphere and that the exsolution of DIC during decrepitation does not meaningfully contribute to the measured CO_2, giving confidence in applying our methods to new and existing analyses of both modern and ancient natural halite. Bulk gas analysis of fluid inclusions is one of the only methods to directly constrain ancient atmospheric composition through deep time and extend the record of atmospheric pCO₂ well beyond the ice cores.

Keywords: Fluid Inclusions, Earth's Ancient Atmosphere, CO_2, Halite

*Corresponding author at: Department of Earth and Environmental Sciences, Rensselaer Polytechnic Institute, Troy, NY, USA. *Email address*: schall@rpi.edu

1. Introduction

Understanding Earth's climate history depends on reconstructing past atmospheric CO_2 concentrations, which relies on indirect geochemical proxies for time periods prior to the ice core record. (Petit et al., 1999; Schaller et al., 2015; CenCO2PIP, 2023). In ancient systems, proxy

76 methods used to estimate pCO_2 (e.g., the $\delta^{13}C$ of pedogenic carbonates and leaf stomatal indices)
77 often show similar trends over the same time interval, but disagree in absolute value (c.f.
78 McElwain et al., 1999; Schaller et al., 2011). Despite these and similar inconsistencies, many of
79 the proxy methods show the expected coherent relationship between relative pCO_2 and
80 temperature on geological timescales, indicating that they are precise but ultimately inaccurate
81 (Knobbe and Schaller, 2018; Tierney et al., 2020; Judd et al., 2024). Addressing this inaccuracy
82 requires direct constraints on ancient atmospheric CO_2, which can be accomplished using fluid
83 inclusions hosted in halite that trap and preserve samples of ancient air. Halite forms in both
84 modern and ancient surficial environments and recent measurements have demonstrated that
85 gases contained within the fluid inclusions in these samples are a direct and high-fidelity archive
86 of Earth's atmospheric composition that may be extended to time periods prior to the ice core
87 record (Blamey et al., 2016; Steadman et al., 2020; Park and Schaller, 2025). Gas analysis of
88 inclusions in halite can be used to validate and refine existing CO_2 proxy records; however,
89 accurate interpretations of inclusion gases requires explicit consideration of phase chemistry
90 (Park and Schaller, 2025).

91 Major atmospheric gases contained within fluid inclusions (e.g., N_2, O_2, Ar, and CO_2) can be
92 quantified via mass spectrometry through mechanical decrepitation under high-vacuum (Graney
93 and Kesler, 1995; Williams, 1996; Norman and Blamey, 2001; Pettitt and Schaller, 2020). Within
94 the past decade, the gas compositions from Proterozoic and Phanerozoic halite have provided
95 direct constraints on ancient atmospheric composition (Blamey et al., 2016; Steadman et al.,
96 2020; Brand et al., 2021). However, these studies have garnered criticism for interpreting raw
97 results (Yeung, 2017; Mills et al., 2023) that contradict prior model predictions and geochemical
98 proxies (Lyons et al., 2014; Catling and Zahnle, 2020). A major issue with these studies is the
99 failure to partition the gaseous from the aqueous phases in their analyses, as they explicitly
100 assume that the volatiles measured are solely from air bubbles within the inclusions, neglecting
101 the contribution of the aqueous phase. Ignoring the volatile contribution from the aqueous phase
102 in inclusion analyses lead to erroneous interpretations of the overlying atmosphere (Park and
103 Schaller, 2025), as the individual gaseous components of the atmosphere are notably different
104 than the aqueous component at equilibrium, due to different solubilities (Yeung, 2017; Pettitt et
105 al., 2020). Park and Schaller (2025) resolved this problem by developing a gas-aqueous
106 partitioning method for fluid inclusion data to apportion the atmospheric volatiles between the
107 gaseous and aqueous phases and determine the equilibrium atmosphere under which the sample
108 had formed (see section 3.5 for more details). This method was validated through analyses of
109 inclusions in halite grown under controlled laboratory conditions, where the partitioned gas data
110 align with gas compositions of the known atmospheric condition (Park and Schaller, 2025). After
111 a robust screening protocol for primary inclusions, this partitioning method can be applied to
112 ancient halite to reconstruct ancient atmospheric CO_2 compositions, showing that the measured
113 gas contents align well with existing models and proxies (Canfield, 2013; Krissansen-Totton et
114 al., 2018; Park and Schaller, 2025). Furthermore, Park and Schaller (2025) demonstrated that
115 only after applying the gas-aqueous partitioning method to Blamey et al's (2016) and Blamey's
116 and Brand's (2019) data does the CO_2 content produce meaningful results, highlighting the
117 necessity of applying the gas-aqueous correction to raw inclusion data.

118 The gas-aqueous partitioning method has changed how we interpret ancient atmospheric
119 compositions from fluid inclusion data and our understanding of the biogeochemical cycling of
120 atmospheric volatiles (Park and Schaller, 2025). However, data generated by bulk gas analysis of
121 fluid inclusions have raised many theoretical and fundamental geochemical questions that, to our
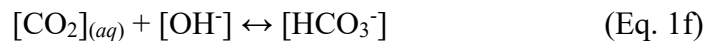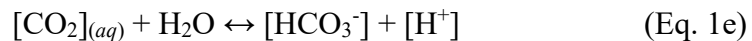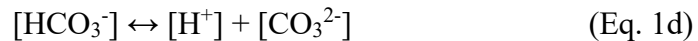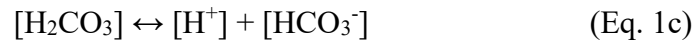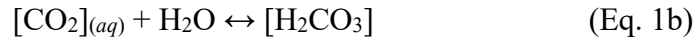
122 surprise, have not been addressed in the literature to date. The current study was inspired by a
123 discussion between the authors and a colleague at the 2023 AGU Annual Meeting on whether the
124 measured CO_2 from bulk gas analysis of inclusions represents $[CO_2]_{aq}$ (as we assumed), or some
125 or all of the Total Dissolved Inorganic Carbon (TDIC) in solution. Delving further into this topic,
126 we found that even basic questions like "what happens to $CO_{2(aq)}$ and HCO_3^- when a solution is
127 rapidly exposed to high vacuum?" have not been addressed. Answering this question is critical
128 for determining whether CO_2 content measured on fluid inclusions truly represents the
129 equilibrium between a brine and the overlying air during mineral formation. Other studies have
130 recognized this problem (Hudgins et al., 2024; Park and Schaller, 2025), and Pettitt et al. (2020)
131 assumed that the measured CO_2 from palustrine cherts from the Petrified Forest National Park
132 (215 Ma) represents TDIC and not a mix between $CO_{2\,(g)}$ and $[CO_2]_{aq}$ (air and air-saturated brine
133 CO_2). During analysis, inclusions hosted in minerals are mechanically decrepitated to release
134 trapped volatiles into a high vacuum environment (10^{-7} to 10^{-8} mbar). Rapid exposure to
135 pressures far below the vapor pressure of the liquid leads to fluid vaporization on millisecond
136 timescales. Pettitt et al. (2020) assumed that the dissolved carbonate species (HCO_3^- and CO_3^{2-})
137 underwent protonation and dehydration reactions before exsolving into CO_2 gas during fluid
138 vaporization. However, this assumption is unverified, and other studies hint that the majority of
139 the HCO_3^- and CO_3^{2-} precipitate as a carbonate salt during rapid depressurization by combining
140 with dissolved metal cations (Cui et al., 2001; McSween et al. 2003).

141 In this study, we test whether the CO_2 content measured from bulk gas analysis in fluid
142 inclusions accurately represents the overlying air at various pCO_2 levels during mineral
143 formation, rather than the exsolution of some or all the TDIC. We hypothesize that the fluid
144 inclusions in halite faithfully record the atmospheric conditions under which the mineral
145 precipitated, and that the measured CO_2 content is derived solely from a mixture of CO_2 in air
146 and $[CO_2]_{aq}$ from air-saturated brine. We predict that an insignificant amount of HCO_3^- and CO_3^{2-}
147 will exsolve into CO_2, because as discussed in section 2, the carbonate reaction kinetics are too
148 sluggish. To address this, we conducted depressurization experiments and bulk gas analysis via
149 mass spectrometry on aqueous salt solutions equilibrated with air, and lab-grown halite that
150 precipitated under controlled pCO_2 atmospheres (450 ppm, 3000 ppm, and 5000 ppm).

151 **2. Theoretical considerations**

152 We can calculate how much $[HCO_3^-]$ and $[CO_3^{2-}]$ transform into CO_2 before inclusion fluid
153 vaporization. If the measured CO_2 content represents the complete exsolution of TDIC, then
154 previous studies have overestimated and misinterpreted their results.

155 The kinetics of the carbonate system equilibrium is essential for understanding the above
156 scenario and is controlled by the following reactions (Kern, 1960):

157 $$CO_{2\,(g)} \leftrightarrow [CO_2]_{(aq)} + H_2O \qquad \text{(Eq. 1a)}$$

158 $$[CO_2]_{(aq)} + H_2O \leftrightarrow [H_2CO_3] \qquad \text{(Eq. 1b)}$$

159 $$[H_2CO_3] \leftrightarrow [H^+] + [HCO_3^-] \qquad \text{(Eq. 1c)}$$

160 $$[HCO_3^-] \leftrightarrow [H^+] + [CO_3^{2-}] \qquad \text{(Eq. 1d)}$$

161 $$[CO_2]_{(aq)} + H_2O \leftrightarrow [HCO_3^-] + [H^+] \qquad \text{(Eq. 1e)}$$

162 $$[CO_2]_{(aq)} + [OH^-] \leftrightarrow [HCO_3^-] \qquad \text{(Eq. 1f)}$$

4

163   In reaction (Eq. 1a), gaseous CO_2 is dissolved in water, and hydrolyzes to carbonic acid (Eq. 1b).
164   Hydrogen ions dissociate from carbonic acid to form a bicarbonate ion (Eq. 1c), and further
165   dissociation forms a carbonate ion (Eq. 1d).

166   The third reaction (Eq. 1c) is considered "instantaneous" (Kern, 1960), and it is impossible to
167   determine whether the hydration reaction occurs directly through the second (Eq. 1b) and third
168   (Eq. 1c) reaction or via the fifth reaction (Eq. 1e) (Eigen et al., 1961). The fifth reaction (Eq. 1e)
169   is sluggish, making it the rate limiting reaction in low pH (<8.2) solutions; however, the sixth
170   reaction (Eq. 1f) is favored at a high pH (>8.2) (Kern, 1960; Johnson, 1982; Dreybrodt et al.,
171   1996). In table 1, k_{+1} to k_{+6} and k_{-1} to k_{-6} are, respectively, the forward and reverse reaction rate
172   constants for the six reactions (Eq. 1a-f).

173   Assuming the reactions (Eq. 1a and e) are being driven to the left by depressurization, we can
174   calculate the concentration of each species of interest (i.e., $[CO_2]_{aq}$ and $[HCO_3^-]$) that will
175   exsolve before fluid vaporization under high vacuum (10^{-7} to 10^{-8} mbar). Based on our
176   observations from the low-vacuum depressurization experiments in this study, complete fluid
177   vaporization during decrepitation is 5 milliseconds (0.0004 L·s^{-1}) (Data availability video). For
178   the reverse reaction of Eq. 1a, the rate is given as:

179
$$-\frac{\partial [CO_2]_{aq}}{\partial t} = k_{-1} \cdot [CO_2]_{aq} \qquad \text{(Eq. 2a)}$$

180   Where $-\partial [CO_2]_{aq}/\partial t$ is the rate in M·s^{-1} and k_{-1} is the reverse kinetic rate constant for Eq.
181   1a (Table 1). Eq. 2a can be integrated to determine the $[CO_2]_{aq}$ at a given time:

182
$$[CO_2]_t = [CO_2]_0 \cdot e^{-k_{-1} \cdot t} \qquad \text{(Eq. 2b)}$$

183   Where $[CO_2]_t$ is the CO_2 concentration at a given time, $[CO_2]_0$ is the starting CO_2
184   concentration, and t is time in seconds. The rate for Eq. 1e is:

185
$$-\frac{\partial [HCO_3^-]}{\partial t} = k_{-5} \cdot [HCO_3^-] \cdot [H^+] \qquad \text{(Eq. 2c)}$$

186   Where $-\partial [HCO_3^-]/\partial t$ is the rate in M·s^{-1} and k_{-5} is the reverse kinetic rate constant for Eq. 1e
187   (Table 1). Eq. 2c can be integrated to determine the $[HCO_3^-]$ at a given time:

188
$$[HCO_3^-]_t = [HCO_3^-]_0 \cdot e^{-k_{-5} \cdot [H^+] \cdot t} \qquad \text{(Eq. 2d)}$$

189   Where $[HCO_3^-]_t$ is the bicarbonate concentration at a given time and $[HCO_3^-]_0$ is the starting
190   bicarbonate concentration. The exsolution of $[CO_3^{2-}]$ likely contributes a negligible amount to
191   $[CO_2]_{aq}$ as $[CO_3^{2-}]$ requires protonation in two reaction steps (Eq. 1c and 1d) and is subsequently
192   dehydrated (Eq. 1b). The exsolution of $[CO_3^{2-}]$ can be ignored as the time required for $[CO_3^{2-}]$ to
193   exsolve into $[CO_2]_{aq}$ exceeds the inclusion fluid vaporization rate. Kinetic constants for this
194   discussion are assumed to be at STP. Pressure effects on the carbonate kinetic rates are crucial to
195   accurately characterize the depressurization of a carbonate solution, yet they are poorly
196   constrained. Eldik and Palmer (1982) and Millero and Berner (1972) suggest that changes in the
197   carbonate system constants are negligible at low pressures (10^{-7} to 10^{-8} mbar). Pressure
198   dependence has been investigated for reaction k_{-2}, showing a negative linear trend, with values
199   indistinguishable between 1000 and 10,000 mbar (Eldik and Palmer, 1982). Moreover, Millero
200   and Berner (1972) show that the carbonate equilibria constants do not change dramatically with
201   decreasing pressure. Therefore, we assume the kinetic constants are similar to those at STP.
202   Using Eq. 2d, we calculate that 0.0003% of the $[HCO_3^-]$ would exsolve into $[CO_2]_{aq}$, after 5
203   milliseconds. Under these conditions, it would take 43 minutes for half of the $[HCO_3^-]$ to exsolve

5

204 into $[CO_2]_{aq}$. Furthermore, the reverse reaction of Eq. 1e is thermodynamically unfavorable, as
205 the forward reaction is spontaneous (Kern 1960). Nonetheless, 0.004% of the $[CO_2]_{aq}$ would
206 dissociate into $[HCO_3^-]$. Therefore, the kinetics of the carbonate system suggest that a negligible
207 amount of $[HCO_3^-]$ would be exsolved into $[CO_2]_{aq}$ during inclusion decrepitation. The
208 remaining $[HCO_3^-]$ and $[CO_3^{2-}]$ should rapidly precipitate as a carbonate salt after solution
209 vaporization.

210 We can estimate how quickly $NaHCO_3$ precipitates during the decrepitation process by
211 applying classical nucleation theory (Mullin, 2001), which is described as follows:

212
$$J = A\ exp\ (-\frac{1}{ln(\Omega)^2}) \qquad \text{(Eq. 3a)}$$

213 Where J is the rate of nucleation, A is the pre-exponential factor (or the frequency of
214 molecular collisions), and Ω is the solution saturation index. In our context, the solution
215 saturation can be written as:

216
$$\Omega = \frac{[Na^+][HCO_3^-]}{K_{sp\ (NaHCO3)}} \qquad \text{(Eq. 3b)}$$

217 Where $K_{sp\ (NaHCO3)}$ is the solubility constant for $NaHCO_3$ (Drever, 1997). A solution $\Omega > 1$
218 indicates that the solution is saturated with respect to the products. From Eq. 3a, the rate of
219 nucleation is controlled by the degree of saturation. As saturation increases, the nucleation rate
220 increases rapidly until $NaHCO_3$ salt precipitates. With the near instantaneous vaporization of the
221 inclusion fluid, the solution becomes supersaturated almost instantaneously, causing the HCO_3^-
222 and CO_3^{2-} to precipitate as a carbonate salt by combining with the dissolved metal cations. Given
223 the rapid vaporization time compared to the slow carbonate equilibrium kinetics, the exsolution
224 of $[HCO_3^-]$ and $[CO_3^{2-}]$ would contribute a negligible amount to the measured CO_2 content.

225 **3. Methods**

226 *3.1. Preparation of stock solutions*

227 A 0.25 M $NaHCO_3$ solution and a 3.5 wt% Instant Ocean Sea Salt solution (spectrum brand)
228 were made with Millipore water (18 MΩ·cm) and allowed to equilibrate with laboratory
229 atmosphere. Solution pH, temperature, and overlying pCO_2 were measured prior to experiments
230 on an Oakton pH 150, a ThermoPro TP50 Digital hygrometer and thermometer, and an Aranet4
231 CO_2 meter, respectively. The Aranet4 CO_2 meter uses a nondispersive infrared sensor to measure
232 the concentration of CO_2. The 3.5 wt% Instant Ocean Sea Salt solution was used to replicate
233 modern ocean water conditions as it is an excellent comparison (Pretet et al., 2014). The
234 carbonate species were calculated using the carbonate open system equations (Drever, 1997).

235 *3.2. Low-vacuum depressurization experiments*

236 To test whether rapid fluid vaporization of a carbonate solution leaves behind the expected
237 mass of carbonate salt and to visually observe complete fluid vaporization, we performed
238 depressurization experiments by placing 2 and 25 microliters of the 0.25 M $NaHCO_3$ solution
239 inside a microcapsule using a syringe (Hamilton). The microcapsules were filled and placed in a
240 glass vial connected to an ultratorr on a vacuum line, with temperature and pressure measured
241 before the solution was exposed to a vacuum of 10^{-3} mbar (Fig. 1). The glass vial was exposed to
242 vacuum until the solution in the microcapsule evaporated and the pressure stabilized. A video of
243 the experiment being conducted in a capillary tube is available in the data availability section.
244 After the vacuum experiment, the microcapsule was retrieved and weighed on a microbalance to

245 determine the mass of the resulting $NaHCO_3$ salt. The 25 μL experiments were conducted in the
246 same manner as the 2 μL experiments.

247   Gravimetric measurements of the stock solution in the microcapsule proved challenging
248 because rapid evaporation of the small volumes of water prevented the microbalance from
249 stabilizing, hindering accurate determinations of the amount of $NaHCO_3$ in individual
250 experiments necessary for mass balance purposes. Instead, the average mass of the 2 μL and 25
251 μL stock solutions was determined gravimetrically by using the syringe to repeatedly decant the
252 2 μL and 25 μL solutions into an enclosed tin capsules to prevent evaporation; the mean of the 2
253 μL solution from the syringe was $\bar{x}$ =1.92 mg (2σ = 0.23; n = 25) and mean of the 25 μL was $\bar{x}$ =
254 25.19 (2σ = 0.34; n = 10).

255 *3.3. Lab-grown halite crystals*

256   Halite crystals were grown from NaCl (Fisher Science Education Brand: S25541) dissolved
257 in Millipore water (18 MΩ·cm) under three experimental treatment conditions: one under normal
258 laboratory pCO_2 conditions and two under elevated pCO_2 conditions (~3000 and ~5000 ppmV).
259 Halite precipitated under open lab conditions formed under variable pCO_2 of 774 ± 23 to 384 ±
260 12 ppm. This batch of halite precipitated under a temperature range of 23 ± 0.4°C to 26.7 ±
261 0.4°C. CO_2 was monitored using an Aranet4 CO_2 meter. Additionally, halite crystals were grown
262 under normal laboratory conditions with a 0.01 M $NaHCO_3$ solution added to the NaCl saturated
263 water. Clean beakers and petri dishes were used to prevent biological material from altering the
264 trapped gas chemistry. Halite precipitation at elevated pCO_2 was achieved by placing NaCl
265 saturated water into a sealed pressure vessel, which is designed to maintain unique atmospheric
266 gas compositions (Fig. 1). The saturated halite solution was then placed inside the pressure
267 vessel, sealed, and then purged with 'zero' grade dry air (Airgas) to remove the humidity and
268 reduce the CO_2 concentration to near zero (Appendix Fig. S1). Following purging, 1000 mbar of
269 zero grade air was injected into the pressure vessel to simulate the modern major atmospheric
270 gas composition, as it is comparable (78.5 ± 2% N_2, 21.5 ± 2% O_2, balanced Ar; Airgas, Radon,
271 PA, USA), minus humidity and CO_2. The CO_2 content was controlled by injecting medical grade
272 CO_2 (Airgas) into the pressure vessel using a low-pressure regulator. CO_2 levels were monitored
273 using the Aranet4 CO_2 meter placed inside the pressure vessel (Fig. 1). Two batches of halite
274 crystals were precipitated under two elevated pCO_2 conditions. The first batch precipitated over a
275 few days under a maximum pCO_2 of 3568 ± 107 and a minimum pCO_2 of 3020 ± 91 ppm, and a
276 temperature range of 17.6 ± 0.4°C to 20.1 ± 0.4°C. The second batch precipitated under a
277 maximum pCO_2 of 5329 ± 160 and a minimum 4705 ± 141 ppm at temperature range of 18.5 ±
278 0.4°C to 20.6 ± 0.4°C. During halite precipitation, pressure and humidity were also monitored
279 using the Aranet4 CO_2 meter (Appendix Fig. S2). In the halite samples, gas solubility is
280 primarily influenced by sodium and chlorine ions. Although, other cations and anions are likely
281 present, their impact on gas solubility is considered negligible and therefore excluded (Hermann
282 et al., 1995). The precipitated halite contains both primary and gaseous fluid inclusions.

283 *3.4. Measuring volatile contents from fluid inclusions in halite and stock solutions by mass*
284 *spectrometry*

285   Following the methods of Pettitt and Schaller (2020) and Park and Schaller (2025), 60 to 120
286 milligrams of lab-grown halite was loaded into a custom inlet, and mechanically decrepitated to
287 release the trapped gaseous and aqueous volatiles directly into a Pfeiffer Prisma Plus 1-100 amu
288 quadrupole mass spectrometer (QMS). Adsorbed gases were removed from the samples by

7

289 pumping them to a high vacuum (10^{-7} to 10^{-8} mbar). 0.2 microliters of 3.5 wt% Instant Ocean salt
290 and 0.25 M NaHCO$_3$ solutions were loaded into a calibrated pipet volume using a syringe
291 (Hamilton). The solution volume fully occupied the pipet to achieve a minimal amount of
292 headspace. To isolate the solutions from the high vacuum inlet, a cobalt alloy ball stem tip
293 (Swagelok) is compressed onto the mating surface of the volume pipet, forming a gas-tight seal
294 (Pettitt and Schaller, 2020) (Fig. 1). Solutions encapsulated in the pipettes were loaded into the
295 custom inlet, evacuated to high vacuum, and rapidly depressurized, releasing the volatiles
296 through a water trap and directly into the QMS. Similarly, halite samples were crushed into the
297 inlet and the gases were directed through the water trap into the QMS. Upon introduction to the
298 QMS, volatiles produce transient peaks in ion current on a secondary electron multiplier. The
299 quadrupole is tuned to monitor the ion current at m/z 14, 15, 16, 18, 28, 32, 40, and 44 with a 50
300 millisecond dwell time at each nominal mass. M/z 14 is used to quantify N_2^+ due to a mass
301 interference from CO^+ at m/z 28 (Graney and Kesler, 1995; Pettitt and Schaller, 2020). Although,
302 CH_4^+ contributes to m/z 14, its signal is corrected using a separate methane calibration based on
303 calculating the fragmentation from m/z 15 and 16. H_2O^+, O_2^+, Ar^+, and CO_2^+ were measured at
304 m/z 18, 32, 40, and 44, respectively. A cold cathode ion gauge was used jointly with the QMS,
305 and a rise in pressure is observed along with the peaks in ion current. The pressure change is
306 used as a metric for total gas released from each crush. Pettitt and Schaller (2020) show that
307 there is no observable effect of the cold cathode gauge on the measured gas composition as the
308 gauge is active during both calibration and sample analyses.

309   The integrated area of the ion current peak for each species is compared to a calibration curve
310 generated from a calibrated gas mixture and used to quantify the total moles of each gas in the
311 unknown samples. For more details about the instrument setup, calibration method, and
312 measured gas composition errors and reproducibility, consult Pettit and Schaller (2020), Pettitt et
313 al. (2020), and Park and Schaller (2025). Calibration is performed by filling pipette volumes with
314 a dry air standard (78.18±1.56% N$_2$, 20.84±0.42% O$_2$, 0.938±0.019% Ar, and 391.1±7.8 ppm
315 CO$_2$; Airgas, Radnor, PA, USA) at controlled pressures and temperatures, and then releasing the
316 gas into the instrument for quantification (Pettitt and Schaller, 2020). This calibration method
317 simulates the pulsed release of gases during crushing and enables quantification down to the
318 femtomol level.

319 *3.5. Gas-aqueous partitioning of volatiles*

320   The gas phase in the experimental stock solutions corresponds to the headspace when the
321 volume pipet is sealed off with the stem tip (Fig. 1), whereas the aqueous phase is comprised of
322 the dissolved atmospheric gases at equilibrium with the atmosphere at the time of isolation. For
323 inclusions in the lab-grown halite, the gas phase corresponds to the atmosphere under which the
324 halite precipitated, whereas the aqueous phase are the atmospheric gases dissolved at
325 equilibrium. Because of the multiphase nature of these experiments, the composition of the
326 released gases are expected to fall along a spectrum between the fully gaseous and fully aqueous
327 endmembers. Thus, the gas and aqueous composition must be partitioned to determine the true
328 composition of the atmosphere under which the stock solution and lab-grown halite equilibrated.
329 This gas-aqueous partitioning procedure (MAGPI: **M**ethod for **A**tmospheric **G**as **P**artitioning
330 from fluid **I**nclusions) is briefly described below, but consult Park and Schaller (2025) for details
331 on the method development, source code, and assumptions made. Partitioning the gas phase from
332 the aqueous phase is based on the measured gas ratios (e.g., N$_2$/Ar). The gas ratios can be used to

8

333 partition the contributions from both the gaseous and aqueous phases to obtain the true
334 atmospheric composition by using:

335
$$X_j^{atm} = \frac{n_j^{obs}}{\left(\frac{\varphi_g}{RT}+(1-\varphi_g)H_S^i(T,S)\right)}\left[\sum_{i=1}^{M}\frac{n_i^{obs}}{\left(\frac{\varphi_g}{RT}+(1-\varphi_g)H_S^i(T,S)\right)}\right]^{-1}$$
(Eq. 4)

336   Where X_j^{atm} is the mole fraction of the atmospheric component of the volatile of interest;
337 n_j^{obs} is the moles observed of the volatile of interest; M are the volatiles taken into consideration
338 (N_2, O_2, Ar, and CO_2); n_i^{obs} is the moles of gas i observed in the analysis; φ_g is the gas volume
339 fraction calculated from the N_2/Ar ratio; R is the universal gas constant; T is the temperature of
340 the fluid inclusion in Kelvin; H_S^i is the temperature and salinity dependent Henry's solubility
341 constant of the gas of interest; and S is the salinity of the fluid inclusion. The solubility of each
342 gas is dependent on the temperature and the salinity of the brine (Onda et al., 1970; Hermann et
343 al., 1995). MAGPI was used to perform the calculations on all the decrepitation and
344 depressurization data present in this study. Our measured gas contents are reported with
345 uncertainties at the 95% confidence interval. Errors are propagated using standard techniques
346 following Ku (1996).

347 *3.6. Raman spectroscopy*

348   Raman spectroscopy is employed to meet several objectives: 1. To test whether the residue
349 from the low-vacuum depressurization experiment is $NaHCO_3$ salt; 2. To determine inclusion
350 salinity so that an accurate Henry's solubility constant is used for calculating the gas volume
351 fraction; and 3. To further validate that the fluid inclusions in lab-grown halite capture the
352 overlying atmosphere during precipitation by analyzing gas dominated inclusions. Salinity
353 calibration and inclusion analysis were performed on a Horiba XploRA confocal Raman
354 spectrometer at Rensselaer Polytechnic Institute (RPI) following the calibration technique of Sun
355 et al. (2010), described below. Analysis of the experimental residue was performed on a Bruker
356 Senterra Raman spectrometer at RPI. Measurements on both instruments use a 532 nm green
357 laser at 20 mW power. Using a 600-diffraction grating, measurements were made with a 50x
358 objective and a 50 μm aperture at 2 cm^{-1} spectral resolution. Experiments were integrated for 30
359 seconds with 3 accumulations. Analysis of the gas dominated inclusion used a 1200-diffraction
360 grating and was integrated for 300 seconds with 3 accumulations. Raman spectra were exported
361 to OriginPro graphing and analysis software and background corrected.

362   We performed laser Raman spectroscopy on the low-vacuum experimental residue to
363 determine whether the residue is in fact $NaHCO_3$ salt in either the amorphous or the expected
364 crystalline form. $NaHCO_3$ has four main Raman active bands, where weak bands occur at 688
365 cm^{-1} (v_4, in-plane deformation) and 1432 cm^{-1} (v_3, C–O antisymmetric stretch), a medium
366 strength band at 1271 cm^{-1} (v_1, C–O symmetric stretch), a very strong band at 1048 cm^{-1} (v_1, C–
367 O symmetric stretch), and eight translational lattice bands between 80-250 cm^{-1} (Frezzotti et al.,
368 2012). We compared the spectra of the experimental residue to the original $NaHCO_3$ salt as well
369 as to the glass microcapsule.

370   Accurate temperature and salinity data are essential for calculating Henry's solubility
371 constants for each volatile species (N_2, O_2, Ar, and CO_2), and are necessary inputs to the gas-
372 aqueous partitioning calculation using MAGPI (Park and Schaller, 2025). The temperatures of
373 the stock solutions and the lab-grown halite were recorded prior to gas analysis of the samples.
374 Stock solution salinity was determined from the added constituents. The salinity of the fluid

9

inclusions in halite was quantified through Raman spectroscopy by following the method of Sun et al. (2010), which quantifies [Cl⁻] in the inclusion and can be converted to an equivalent NaCl salinity. Salinity of the NaCl solution was determined via Raman spectroscopy rather than relying on the initial aqueous concentrations because evaporation during halite precipitation increases brine salinity to an unknown value (Lowenstein et al., 2001). The salinity of the trapped brine in the inclusion is the salinity of the brine at the time of precipitation, and determination via Raman spectroscopy is a reliable and accurate method to quantify inclusion salinity in the lab-grown halite (He et al., 2024; Sun, 2009; Sun et al., 2010). [Cl⁻] was estimated based on the relative intensity changes of the two deconvoluted peaks at 3220 cm⁻¹ and at 3450 cm⁻¹ in the OH⁻ stretch for H_2O, relative to the corresponding peaks for pure H_2O. Deconvolution was performed in the OriginPro graphing and analysis software. The average salinity of the lab-grown halite is ~39 wt% (~6.7 mol/L of NaCl) (Appendix Fig. S3).

We further validate the assertion that inclusions in halite trap samples of atmospheric gases during mineral formation by *in-situ* analysis of a gas-dominated inclusion using laser Raman spectroscopy. This was accomplished by comparing the atmospheric N_2/O_2 ratio under which the lab-grown halite precipitated to the N_2/O_2 intensity ratio of the gas trapped within the inclusion. The similar Raman cross-sections between N_2 and O_2 allow their Raman intensities to facilitate direct comparisons between N_2 and O_2 trapped within the inclusion (Fouche and Chang, 1971; Fenner et al., 1973). N_2 has one strong Raman active band at 2331 cm⁻¹ (N≡N stretch) and O_2 has one strong Raman active band at 1555 cm⁻¹ (O=O stretch) (Burke, 2001; Frezzotti et al., 2012). Further comparisons were made between the measured N_2/O_2 values from the bulk gas analyses and the N_2/O_2 intensity ratios obtained by the Raman spectrometer. Both the Raman spectra and the gas analyses are expected to reflect the injected N_2/O_2 ratio of 3.73 ± 0.2, a value similar to the modern atmosphere (Brimblecombe, 1996). The birefringence of the halite should not affect the quantification of N_2 and O_2, as halite is isotropic and does not influence the Raman peak intensities of interest (Caumon et al., 2015). Furthermore, a confocal Raman spectrometer was used, which bypasses the halite crystal ensuring that is does not contribute to the analysis (Fries and Steele, 2011).

4. Results

4.1. Low-vacuum depressurization experiments of a carbonate solution

Masses of the residues resulting from the low-vacuum depressurization experiments fall on the 1:1 line for both the 2 μL ($\bar{x}$ = 0.043 mg; σ = 0.003; n = 10) and 25 μL ($\bar{x}$ = 0.523 mg; σ = 0.009; n = 2) volumes, and are within the expected syringe-mass procedural error (2 μL; 0.043 mg ± 0.003, and 25 μL; 0.525 mg ± 0.014) (Fig. 2 and Table 2). Our experimental results do not noticeably deviate from the expected yields based on calculations in section 3.2, suggesting that the majority of HCO_3^- and CO_3^{2-} does not transform into CO_2. Although, the amount of CO_2 released could not be quantified as the equipment used did not have enough significant figures to accurately quantify the expected CO_2 loss gravimetrically, CO_2 was quantified during the depressurization and decrepitation experiments performed on the QMS.

Peaks in the Raman spectra of the experimental residue match those in the spectrum of the original $NaHCO_3$ salt (Fig. 3), confirming that the residue is the original carbonate salt (and is distinct from glass microcapsule). The main Raman bands are observed at 688 cm⁻¹, 1048 cm⁻¹, and 1271 cm⁻¹, matching those of $NaHCO_3$ (Frezzotti et al., 2012). Additional Raman bands occur at 1017 cm⁻¹ and 1064 cm⁻¹ corresponding to HCO_3^- and CO_3^{2-}, respectively (Davis and

10

419 Oliver, 1972). However, the weaker HCO_3^- band at 1360 cm^{-1} is not present within the residue
420 spectra (Frezzotti et al., 2012). The residue's translational lattice band structure is consistent with
421 that of $NaHCO_3$, indicating that the residue is crystalline. However, the broadening of the
422 spectral bands at 1048 cm^{-1} and within the translational lattice range at 228 cm^{-1}, 205 cm^{-1}, 166
423 cm^{-1}, 153 cm^{-1}, 145 cm^{-1}, 114 cm^{-1}, and 92 cm^{-1} suggest that some of the residue is amorphous. A
424 partly amorphous structure of the experimental residue is likely a consequence of rapid $NaHCO_3$
425 precipitation during solution vaporization, and therefore consistent with our initial hypothesis.

426 *4.2. Quadrupole mass spectrometry depressurization and decrepitation experiments*

427 Quadrupole mass spectrometry was used to quantify the abundance of the major atmospheric
428 gases in the stock solutions and lab-grown halite. We observe mole fractions that lie between the
429 air and air-saturated brine (ASB) endmembers with varied gas volume fractions (Appendix Fig.
430 S4). The measured CO_2 mol percent (mol%) and CO_2 normalized to argon (CO_2/Ar) were both
431 compared to expected values calculated using the partial pressure and aqueous solubility of each
432 gas, the gas volume fraction (φ_g), and the temperature and salinity of the solution. φ_g was
433 obtained from the measured N_2/Ar ratios. Assuming that the gas content solely originates from
434 an air-ASB mixture, the expected molar abundance of each gas of interest is calculated using the
435 following equation:

436
$$n_j^{calc} = P_i V \left[\frac{\varphi_g}{RT} + (1 - \varphi_g) H_s^i(T, S) \right]$$
(Eq. 5)

437   From the calculated expected molar abundance, an expected CO_2 mol% and CO_2/Ar for a
438 given gas volume fraction can be estimated, allowing for comparisons with the measured CO_2
439 content. Where n_j^{calc} is the number of mols for each gas of interest; P_i is the partial pressure of
440 the gas of interest where pN_2, pO_2, pAr was set to 0.7808, 0.2095, and 0.093, while pCO_2 was
441 adjusted to the measured pCO_2 values from the Aranet4. Solubility constants were adjusted to the
442 measured temperature and salinity values. The measured vs expected CO_2% and CO_2/Ar show a
443 linear relationship that closely aligns with the 1:1 slope corresponding to CO_2 derived solely
444 from an air-ASB mixture (Fig. 4 and consult Table 3 for regression equations). We statistically
445 evaluate whether the measured versus expected averages and slopes deviate from the 1:1 using
446 both analysis of variance (ANOVA) and analysis of covariance (ANCOVA) tests. ANOVA
447 compares the averages of two or more groups by analyzing variance, while ANCOVA compares
448 the regression slopes of two or more groups by analyzing the means of the dependent variable
449 (McDonald, 2014). The averages and slopes of the measured CO_2% and CO_2/Ar are statistically
450 indistinguishable from the 1:1 line (Fig. 4 and consult Table 3 for statistics). However, there is a
451 statistically significant deviation of the CO_2/Ar slope from the slope of the 1:1 line based on the
452 ANCOVA test (F=6.56; p(α)=0.01). This deviation may be due to the argon normalization
453 slightly shifting the slope from the 1:1 line. However, the confidence interval for the CO_2/Ar
454 slope overlaps with the 1:1 line (Fig. 4).

455   Using equation 4, a unique correction was applied to each of the stock solutions and lab-
456 grown halite analyses (Park and Schaller, 2025). The raw data was partitioned into their gaseous
457 and aqueous endmembers to determine the atmospheric composition that each equilibrated under.
458 When partitioned, the N_2, O_2, and Ar accurately reflect the modern atmosphere and the
459 atmosphere used inside the pressure vessel (Appendix Fig. S5). The partitioned CO_2 from the
460 lab-grown halite that precipitated under "normal" and elevated pCO_2 fall within the expected
461 pCO_2 range of their respective conditions (Fig. 5 and Table 4). Because laboratory pCO_2 is
462 variable, the pCO_2 with which the stock solutions had equilibrated was recorded before the setup

463 of each depressurization experiment. The partitioned CO_2 from the stock solutions falls along the
464 expected 1:1 line corresponding to pCO_2 measured by the Aranet4. CO_2% and CO_2/Ar of the
465 unpartitioned and partitioned gases from the stock solutions and lab-grown halite are compared
466 to each other and shown in Fig. 6 and values are in Table 5.

467 *4.3. Depressurization and total dissolved inorganic carbon*

468   To test whether the measured CO_2 solely represents air-ASB CO_2 or the exsolution of TDIC,
469 we modeled the expected CO_2 content for both end-member scenarios over a range of gas
470 volume fractions (φ_g). The modeled CO_2% and CO_2/Ar for an air-ASB mixture were calculated
471 using equation 5. In contrast, the complete TDIC exsolution model was generated by estimating
472 TDIC from the measured pH, pCO_2, temperature, and salinity of each solution, using the open
473 carbonate system equations (Drever, 1997). For this model, we assumed that the TDIC
474 completely exsolved into $CO_{2\ (aq)}$, and the resulting $CO_{2\ (aq)}$ was used with the appropriate
475 Henry's constant in equation 5. The solubility constants were adjusted to the measured
476 temperature, salinity, and whether the solution was NaCl or $NaHCO_3$ dominated, producing a
477 unique CO_2 model for each stock solution (Hermann et al., 1995). We then compared the
478 measured CO_2 content from each stock solution to the modeled expectation as a function of φ_g
479 (Fig. 7). The measured CO_2% (<1%) and CO_2/Ar (<1) values are consistent with the air-ASB
480 CO_2 model at the measured gas volume fraction range (0.01-0.12). In contrast, the complete
481 exsolution of TDIC model yields CO_2 75 ± 15% and 500 ± 354 CO_2/Ar for the same gas volume
482 fraction range (Fig. 7). TDIC exsolution models were not calculated for the lab-grown halite, as
483 the inclusion pH could not be estimated. Although we attempted to quantify inclusion pH using
484 the Raman method of Hudgins et al. (2024), it was unsuccessful at these concentrations.
485 However, if we assume that the initial pH of the halite solution reflects the inclusion pH, the
486 measured lab-grown halite CO_2 content aligns with the air-ASB CO_2 model for a given φ_g
487 (Appendix Fig. S6).

488 *4.4. Raman spectra of a gas dominated lab-grown inclusion*

489   Raman analysis on a gas dominated inclusion shows the main peaks for N_2 and O_2 present at
490 2331 cm^{-1} and 1555 cm^{-1} (Burke, 2001; Frezzotti et al., 2012) (Fig. 8). Ratioed peak intensities
491 of N_2 and O_2 (I_{N2}/I_{O2}) give a value of 3.84 ± 0.2, which closely aligns with the atmospheric value
492 under which the halite precipitated (3.73 ± 0.2), and is distinct from the aqueous end-member
493 ratio of 1.73 ± 0.2. Furthermore, the I_{N2}/I_{O2} is in range with the partitioned N_2/O_2 contents of the
494 lab-grown halite and stock solutions bulk gas analyses ($\bar{x}$ = 3.78 ± 0.24) (Fig. 9). This suggests
495 that direct N_2/O_2 measurements can be obtained prior to the ice core record via Raman
496 spectroscopic methods (Ikeda et al., 1999; Ohno et al., 2021). Future hypothesis testing should
497 focus on measuring N_2/O_2 in natural samples, and testing whether N_2 or O_2 is excluded during
498 halite crystallization, similar to the ice core record (Severinghaus and Battle, 2006). However, in
499 our analysis, it does not appear that the lab-grown halite preferentially incorporates any one gas
500 during crystallization.

501 **5. Discussion**

502 *5.1. CO_2 from inclusion analysis is a mix of air and air-saturated brine*

503   The measured CO_2 from the depressurization and decrepitation experiments are in close
504 agreement with the expected endmembers of air-ASB, and not the complete or even partial
505 exsolution of TDIC (Fig. 4, 6, 7). This is supported by the statistically identical averages and

slopes of the expected versus measured CO_2 (Fig. 4 and Table 3), and the large differences between the measured CO_2 content and the complete TDIC exsolution model (Fig. 7). Our data is also consistent with the kinetics of the carbonate system equilibria, showing that equilibrium is too sluggish to allow exsolution of a substantial amount of HCO_3^- or CO_3^{2-} during fluid inclusion decrepitation. During fluid vaporization, the $[HCO_3^-]$ and $[CO_3^{2-}]$ become super saturated, causing rapid nucleation of carbonate salts (Mullin, 2001). Therefore, a carbonate salt residue should be observed after both the low-vacuum and QMS depressurization experiments. As shown in section 4.1, the white residue remaining in the microcapsule following the low-vacuum experiments has a Raman spectrum consistent with $NaHCO_3$ salt, and the masses of the salts confirm that a quantitative conversion occurred (Fig. 2 and 3). The mass of the residue around the rim of the volume pipets following the QMS depressurization experiment was not collected, because the volume pipet greatly exceeds the mass limitation of the RPI microbalance. However, the 0.25 M $NaHCO_3$ solution was used in both the low-vacuum and depressurization experiments, and we interpret the white residue around the rim of the volume pipet to be $NaHCO_3$ salt based on the Raman spectra collected from the low-vacuum experiments. Carbonate salt precipitation following boil off of the solution water is supported by experiments on 1 wt% Na_2CO_3 and $NaHCO_3$ solutions (Cui et al., 2001). However, Cui et al. (2001) did not measure the mass of the residue to confirm a quantitative conversion had occurred, and these experiments were conducted at ca. 1 atm, not under vacuum.

Further evidence that the carbonate system equilibria is slower than the rate of carbonate-salt precipitation comes from the equilibration time of a 0.5 M $NaHCO_3$ solution prepared to determine the equilibration time of a carbonate solution to a new atmospheric condition (Fig. 10) (Kern, 1960; Hudgins et al., 2024). Desired weights of $NaHCO_3$ were placed in 50 mL centrifuge tubes and continuously mixed with 50 mL of Millipore water (18 $M\Omega \cdot cm$) until fully dissolved. To ensure the solution reached equilibrium with the laboratory atmosphere, the pH was monitored until the values plateaued. The solution reached equilibrium in approximately 3 hours (Fig. 10), suggesting that an inclusion does not have enough time to equilibrate before rapid vaporization.

In the short time between rupturing a fluid inclusion, but before fluid vaporization, partial exsolution of TDIC could occur in principle, and could contribute to the measured CO_2 content, potentially inflating measured CO_2 values. To explore this possibility, we theoretically estimate the magnitude of this contribution to the measured CO_2 content. Within the 5 milliseconds to boil off the inclusion fluid during decrepitation, 0.0003% of the $[HCO_3^-]$ would be converted to $[CO_2]_{aq}$ via the reverse reaction of Eq. 1e (Kern, 1960). Although, the reverse reaction of Eq. 1e is thermodynamically unfavorable (Drever, 1997), 0.004% of $[CO_2]_{aq}$ would contribute to $[HCO_3^-]$ via the forward reaction. These contributions are exceedingly small compared to the relative error of the CO_2 measurements in our analysis, which was determined from the 95% confidence intervals ($\bar{x} = 6.4\%$; $\sigma = 5.1\%$). Therefore, the potential contribution of partial TDIC exsolution to the measured CO_2 content is indistinguishable from the instrument uncertainty and does not merit correction.

Uncertainty on the measured CO_2 content and minor deviations from the 1:1 line (Fig. 4) cannot be explained by partial DIC exsolution but may be due to limitations of the analytical technique. The CO_2 content is often quantified close to its femtomol limit of detection, which may account for some of the variation between the expected versus measured (Pettit and Schaller, 2020). Furthermore, the effects of solubility are the greatest for CO_2, as its high

551 solubility results in the most significant compositional differences between the gaseous and
552 aqueous phases. Uncertainty in φ_g will disproportionately affect CO_2 relative to the other gases
553 (Park and Schaller, 2025). Another contributing factor to the error and deviation of CO_2 is likely
554 the variability of the pCO_2 levels measured by the Aranet4, as the associated error of the pCO_2
555 increases with higher partial pressure (0-2000 ppm $\pm$ 3% and 2001-9999 $\pm$ 10%).

556   Prior to gas-aqueous partitioning, the measured CO_2 content of the lab-grown halite and
557 stock solutions fall between the expected endmembers of an air-ASB mixture (Fig. 4). However,
558 because CO_2 is highly soluble, interpreting unpartitioned CO_2 from multiphase inclusions as the
559 atmospheric condition will lead to erroneous conclusions. For example, the unpartitioned CO_2
560 content of halite grown at ~3000 ppm could be interpreted as having an average pCO_2 of 112,851
561 $\pm$ 61,200 ppm (Table 4). In contrast, partitioning the same data yields an average pCO_2 of 2992 $\pm$
562 212 ppm, which closely matches the measured pCO_2 the halite precipitated under (Fig. 5 and
563 Table 4). This trend is consistent in the measured CO_2 content, as well as the other gaseous
564 species, in the lab-grown halite and stock solutions (Fig. 5 and 6, Table 4, and Appendix Fig. S5).
565 These findings reinforce that gas-aqueous partitioning is an essential step in inclusion gas
566 analyses to accurately reconstruct atmospheric conditions.

5.2. Biological influences on fluid inclusions in halite

568   The variability within our data could also be caused by biological processes (e.g.,
569 photosynthesis and respiration) altering the O_2 and CO_2 gas chemistry of the fluids trapped
570 within the inclusions, resulting in a gas composition that departs from the expected atmospheric
571 conditions. Although this is a far greater concern on natural samples as complex organic
572 molecules and living microorganisms have been observed in fluid inclusions (Vreeland et al.,
573 2000; Mißbach et al., 2021; Schreder-Gomes et al., 2022), it is possible that microorganisms and
574 organic matter could have been trapped in fluid inclusions during precipitation of the lab-grown
575 halite, altering the gas chemistry. Despite methodological efforts to avoid this, Raman
576 spectroscopy can verify the presence or absence of trapped organic matter or microorganisms.
577 Raman spectra of fluid inclusions from the lab-grown halite do not show peaks associated with
578 organic molecules (Appendix Fig. S7) (Fries and Steele, 2011; Lu et al., 2011). However, it is
579 possible that organic matter or microbes were not detected by the Raman spectrometer if the
580 analyte of interest was below the limit of detection. An additional test to determine biological
581 influence on the lab-grown halite data follows the method of Park and Schaller (2025). To
582 determine if the O_2 and CO_2 measured is influenced by the expected stoichiometric exchange due
583 to photosynthesis or respiration, the expected molar abundance of each gas is calculated relative
584 to the observed moles of N_2 and compared to what is observed. The difference between the
585 observed and expected moles of the two gases can be calculated through the gas-aqueous
586 partition:

587 $$\Delta n_j = n_j^{obs} - \left(\frac{X_j^{atm}}{X_{N_2}^{atm}} * n_{N_2}^{obs} \frac{\left(\frac{\varphi_g}{RT} + (1-\varphi_g)H_s(T,S) \right)_j}{\left(\frac{\varphi_g}{RT} + (1-\varphi_g)H_s(T,S) \right)_{N_2}} \right) \qquad \text{(eq. 6)}$$

588 Where j is the gas of interest, the X_j/X_{N2} term is set to reflect the ratios of the modern
589 atmosphere. Excesses and deficits of O_2 and CO_2 can be compared by plotting the ΔO_2 and
590 ΔCO_2. If photosynthesis or respiration has modified the inclusion gases, then a 1:1 inverse
591 relationship between the gases should be observed. The deficits and excesses in CO_2 and O_2 do
592 not exhibit clear trends indicative to photosynthesis or respiration (Fig. 11). Although, the causes

593 of the deficits and excesses remain unclear, partitioning the gas data accurately reflects the
594 expected atmospheric conditions under which the mineral precipitated and stock solutions
595 equilibrated (Fig. 5, 6, and 9). The larger deficits and excesses observed in the stock solutions
596 relative to the lab-grown halite are due to the physically larger sample volume.

597 *5.3. Inclusions in halite capture a 'snapshot' of the atmosphere*

598 By analyzing air bubbles trapped in glacial ice, the Antarctic ice core record has provided
599 direct compositional measurements of the atmosphere of the last 800 Ka with some isolated
600 intervals dating back to 2 million years (Lüthi et al., 2008; Higgins et al., 2015; Yan et al., 2019).
601 Prior to the ice core record, reconstructing Earth's ancient atmospheric composition has relied on
602 models and a variety of proxy methods that often disagreed in overall trends and absolute values
603 for pCO_2 (CenCO2PIP, 2023). However, as shown by this study and Park and Schaller (2025),
604 inclusions in lab-grown halite clearly trap atmospheric gases during mineral precipitation, where
605 the halite precipitated under controlled atmospheric conditions align with gas compositions
606 introduced into the growth chamber (Fig. 5) (Appendix Fig. S5). Although, Park and Schaller
607 (2025) grew halite in laboratory conditions, this study better controlled the atmospheric
608 conditions during halite precipitation using a sealed pressure vessel. Notably, the halite that
609 precipitated under different CO_2 conditions show distinct CO_2 separation of their respective
610 atmosphere when partitioned. In addition, Raman spectra of a gas dominated inclusion provides
611 secondary evidence that the inclusions in halite trap the atmosphere during mineral formation
612 and are further corroborated with the partitioned N_2/O_2 gas data (Fig. 8 and 9).

613 Bulk gas analyses of inclusions trapped in halite have the potential to extend direct
614 atmospheric compositional (and isotopic) constraints beyond the ice core record (Goldstein,
615 2001), as this study further confirms that CO_2 and O_2 can be directly quantified and partitioned
616 to reflect the true atmosphere during halite formation (Park and Schaller, 2025) (Appendix Fig.
617 S5). This approach can be used to test Earth's degassing history, as well as the evolution and
618 interplay between the atmosphere, biosphere, lithosphere, and hydrosphere. Specifically, this
619 approach can test whether continental weathering can be the main control of long term pCO_2
620 levels (Kent and Muttoni, 2013; Schaller et al., 2015), the relationship between the global mean
621 temperature and increasing pCO_2 (Caballero and Huber, 2013), and whether the $\delta^{13}C$ of mantle
622 derived CO_2 has been consistent or varied throughout Earth history (Des Marais and Moore,
623 1984; Krissansen-Totton et al., 2021). For example, measured $\delta^{13}C$ values of CO_2 trapped in
624 halite inclusions from the Mesoproterozoic Sibley halite (Ontario, Canada) could be used to test
625 the stability of atmospheric $\delta^{13}C$ through the last 1.4 Ga. Further, these values could be used to
626 predict the $\delta^{13}C$ of calcite formation and compared to the value of contemporaneous marine
627 carbonates (Krissansen-Totton et al., 2015). This approach outlines how bulk gas analysis of
628 inclusions in halite have the potential to address unresolved questions that are crucial for
629 quantitative long-term global carbon cycle models and future CO_2 projections (Berner et al.,
630 1983; Foster et al., 2017).

631 Extending the record of Earth's atmospheric CO_2 content beyond the ice cores has heretofore
632 relied on proxies, where the physical, biological, or geochemical property of a fossil or mineral
633 responds to or records some function of the concentration of CO_2 during formation (Royer,
634 2014). However, inclusions in halite have the potential to extend the direct CO_2 record beyond
635 the temporally restricted ice cores (Yan et al., 2019), as we have shown that halite trap gases that
636 are representative of the overlying atmosphere under which they precipitated. Furthermore, the
637 low diffusivity of H_2 and CO_2 through halite at temperatures below 200°C indicates atmospheric

15

gases can be retained within the mineral for billions of years (Zimmermann and Moretto, 1996). Although, post-depositional processes will alter the initial inclusion chemistry, robust screening protocols are used to identify and exclude altered samples, such as, petrography, micro-thermometry, and Raman spectroscopy. See Blamey and Brand (2019), and Brand et al. (2021) for a detailed review of the screening protocol for primary inclusions in halite. Moreover, bulk gas analysis of inclusions is not limited to halite samples as palustrine cherts, soil carbonates, and soil gypsum have produced mole fractions of atmospheric gas compositions that are in excellent agreement with previous model predictions (Pettitt et al., 2020).

6. Conclusions

We test whether the CO_2 content measured from bulk gas analysis in fluid inclusions accurately represents the overlying air at various pCO_2 levels during mineral formation, rather than Pettitt et al's. (2020) assumption that the CO_2 measured represents the complete exsolution of TDIC. We find Pettitt et al's. (2020) assumption to be unsubstantiated. We demonstrate that the CO_2 contents measured in inclusions hosted in halite accurately represents the overlying air at various pCO_2 levels, rather than the complete or partial exsolution of TDIC. Our results show that the measured CO_2 content falls between the expected values of air and air-saturated brine at different CO_2 conditions, and by partitioning gas contributions from each phase, we observe atmospheric pCO_2 values closely matching the conditions under which the lab-grown halite precipitated. These findings demonstrate the ability of halite inclusions to faithfully entrap and preserve atmospheric CO_2 but also the other major atmospheric gases (i.e., N_2, O_2, and Ar), giving us confidence in applying our methods to new and existing analyses of both natural modern and ancient halite-inclusions. Future work should extend this method to other minerals, such as soil carbonates, soil gypsum, and cherts. Bulk gas analysis of fluid inclusions is a promising method to reliably reconstruct the atmospheric composition beyond the ice core record.

CRediT Authorship Contribution Statement

Michael Naylor Hudgins: Conceptualization, Methodology, Formal Analysis, Investigation, Data Curation, Writing – Original Draft, Visualization. **Justin G. Park:** Investigation, Writing – Review & Editing. **Alex M. Ryan:** Investigation, Writing – Review & Editing. **Jessika Rogers:** Investigation, Writing – Review & Editing. **Morgan F. Schaller:** Conceptualization, Resources, Writing – Review & Editing, Supervision.

Data Availability

All data necessary to evaluate the conclusions of this study are available through Mendeley Data at DOI: 10.17632/jzcbs7fjnx.1.

Declaration of Competing Interest

The authors declare that they have no known competing financial interests or personal relationships that could have appeared to influence the work reported in this paper.

Acknowledgements

discussions and to Humberto Terrones for the use of the Raman spectrometer. We are grateful for
the support and help from the CESIA and RARE members.

Appendix A. Supplementary Material

The Supplementary Material to this article can be found online.

References

Berner R. A., Lasaga A. C. and Garrels R. M. (1983) The carbonate-silicate geochemical cycle
and its effect on atmospheric carbon dioxide over the past 100 million years. *Am. J. Sci.*
283, 641–683.

Blamey N. J. F. and Brand U. (2019) Atmospheric gas in modern and ancient halite fluid
inclusions: A screening protocol. *Gondwana Res.* **69**, 163–176.

Blamey N. J. F., Brand U., Parnell J., Spear N., Lécuyer C., Benison K., Meng F. and Ni P.
(2016) Paradigm shift in determining Neoproterozoic atmospheric oxygen. *Geol.* **44**,
651–654.

Brand U., Davis A. M., Shaver K. K., Blamey N. J. F., Heizler M. and Lécuyer C. (2021)
Atmospheric oxygen of the Paleozoic. *Earth Sci. Rev.* **216**, 103560.

Brimblecombe P. (1996) *Air Composition and Chemistry*., Cambridge University Press.

Burke E. A. J. (2001) Raman microspectrometry of fluid inclusions. *Lithos* **55**, 139–158.

Caballero R. and Huber M. (2013) State-dependent climate sensitivity in past warm climates and
its implications for future climate projections. *Proc. Natl. Acad. Sci. U.S.A.* **110**, 14162–
14167.

Canfield D. (2013) Proterozoic Atmospheric Oxygen. *Treatise on Geochemistry: Second Edition*
6, 197–216.

Catling D. C. and Zahnle K. J. (2020) The Archean atmosphere. *Sci. Adv.* **6**, eaax1420.

Caumon M.-C., Tarantola A. and Mosser-Ruck R. (2015) Raman spectra of water in fluid
inclusions: I. Effect of host mineral birefringence on salinity measurement. *J. Raman
Spectrosc.* **46**, 969–976.

Cui Q., Chandra S. and McCahan S. (2001) The Effect of Dissolving Gases or Solids in Water
Droplets Boiling on a Hot Surface. *J. Heat Transf.* **123**, 719–728.

Davis A. R. and Oliver B. G. (1972) A Vibrational-Spectroscopic Study of the Species Present in
the CO2-HzO System. *J. Solution Chem.* **1**, 11.

Des Marais D. J. and Moore J. G. (1984) Carbon and its isotopes in mid-oceanic basaltic glasses.
EPSL **69**, 43–57.

Drever J. I. (1997) *The Geochemistry of Natural Waters: Surface and Groundwater
Environments*., Prentice Hall.

Dreybrodt W., Lauckner J., Zaihua L., Svensson U. and Buhmann D. (1996) The kinetics of the
reaction $CO_2 + H_2O \rightarrow H^+ + HCO_3^-$ as one of the rate limiting steps for the dissolution of
calcite in the system H_2O-CO_2-$CaCO_3$. *Geochim. Cosmochim. Acta* **60**, 3375.

17

Fenner W. R., Hyatt H. A., Kellam J. M. and Porto S. P. S. (1973) Raman cross section of some simple gases. *J. Opt. Soc. Am., JOSA* 63, 73–77.

Foster G. L., Royer D. L. and Lunt D. J. (2017) Future climate forcing potentially without precedent in the last 420 million years. *Nat. Commun.* **8**, 14845.

Fouche D. G. and Chang R. K. (1971) Relative Raman cross section for N_2, O_2, CO, CO_2, SO_2, and H_2S. *Appl. Phys. Lett.* **18**, 579–580.

Frezzotti M. L., Tecce F. and Casagli A. (2012) Raman spectroscopy for fluid inclusion analysis. *J. Geochem. Explor.* **112**, 1–20.

Fries M. and Steele A. (2011) Raman Spectroscopy and Confocal Raman Imaging in Mineralogy and Petrography. In *Springer Series in Optical Sciences* pp. 111–135.

Goldstein R. H. (2001) Clues from Fluid Inclusions. *Science* **294**, 1009–1011.

Graney J. R. and Kesler S. E. (1995) Factors affecting gas analysis of inclusion fluid by quadrupole mass spectrometry. *Geochim. Cosmochim. Acta* **59**, 3977–3986.

He X., Wang W.-Q., Liu Y.-Z. and Sun Q. (2024) Raman Quantitative Measurement on the Cl^- Molarity of H_2O-NaCl-CO_2 System: Application to Fluid Inclusions. *Minerals* **14**, 1121.

Hermann C., Dewes I. and Schumpe A. (1995) The estimation of gas solubilities in salt solutions. *Chem. Eng. Sci.* **50**, 1673–1675.

Higgins J. A., Kurbatov A. V., Spaulding N. E., Brook E., Introne D. S., Chimiak L. M., Yan Y., Mayewski P. A. and Bender M. L. (2015) Atmospheric composition 1 million years ago from blue ice in the Allan Hills, Antarctica. *Proc. Natl. Acad. Sci.* **112**, 6887–6891.

Hudgins M. N., Knobbe T. K., Hubbard J., Steele A., Park J. G. and Schaller M. F. (2024) In situ quantification of carbonate species concentrations, pH, and pCO_2 in calcite fluid inclusions using confocal Raman spectroscopy. *Appl. Spectrosc.* 00037028241275192.

Ikeda T., Fukazawa H., Mae S., Pepin L., Duval P., Champagnon B., Lipenkov V. Ya. and Hondoh T. (1999) Extreme fractionation of gases caused by formation of clathrate hydrates in Vostok Antarctic Ice. *Geophys. Res. Lett.* **26**, 91–94.

Johnson K. S. (1982) Carbon dioxide hydration and dehydration kinetics in seawater. *Limnol. Oceanogr.* **27**, 849–855.

Judd E. J., Tierney J. E., Lunt D. J., Montañez I. P., Huber B. T., Wing S. L. and Valdes P. J. (2024) A 485-million-year history of Earth's surface temperature. *Science* **385**, eadk3705.

Kent D. V. and Muttoni G. (2013) Modulation of Late Cretaceous and Cenozoic climate by variable drawdown of atmospheric pCO_2 from weathering of basaltic provinces on continents drifting through the equatorial humid belt. *Clim. Past* **9**, 525–546.

Kern D. M. (1960) The hydration of carbon dioxide. *J. Chem. Educ.* **37**, 14.

Knobbe T. K. and Schaller M. F. (2018) A tight coupling between atmospheric pCO_2 and sea-surface temperature in the Late Triassic. *Geol.* **46**, 43–46.

Krissansen-Totton J., Arney G. N. and Catling D. C. (2018) Constraining the climate and ocean pH of the early Earth with a geological carbon cycle model. *Proc. Natl. Acad. Sci. U.S.A.* **115**, 4105–4110.

Krissansen-Totton J., Buick R. and Catling D. C. (2015) A statistical analysis of the carbon isotope record from the Archean to Phanerozoic and implications for the rise of oxygen. *Am. J. Sci.* **315**, 275–316.

Krissansen-Totton J., Kipp M. A. and Catling D. C. (2021) Carbon cycle inverse modeling suggests large changes in fractional organic burial are consistent with the carbon isotope record and may have contributed to the rise of oxygen. *Geobiology* **19**, 342–363.

Ku H. H. (1996) Notes on the use of propagation of error formulas. *J. Res. Natl. Bur. Stand.* **70**, 263–273.

Lowenstein T. K., Timofeeff M. N., Brennan S. T., Hardie L. A. and Demicco R. V. (2001) Oscillations in Phanerozoic Seawater Chemistry: Evidence from Fluid Inclusions. *Science* **294**, 1086–1088.

Lu X., Al-Qadiri H. M., Lin M. and Rasco B. A. (2011) Application of Mid-infrared and Raman Spectroscopy to the Study of Bacteria. *Food Bioprocess Technol.* **4**, 919–935.

Lüthi D., Le Floch M., Bereiter B., Blunier T., Barnola J.-M., Siegenthaler U., Raynaud D., Jouzel J., Fischer H., Kawamura K. and Stocker T. F. (2008) High-resolution carbon dioxide concentration record 650,000–800,000 years before present. *Nature* **453**, 379–382.

Lyons T. W., Reinhard C. T. and Planavsky N. J. (2014) The rise of oxygen in Earth's early ocean and atmosphere. *Nature* **506**, 307–315.

McDonald J. H. (2014) *Handbook of biological statistics*., Sparky House Publishing.

McElwain J. C., Beerling D. J. and Woodward F. I. (1999) Fossil Plants and Global Warming at the Triassic-Jurassic Boundary. *Science* **285**, 1386–1390.

McSween H. Y., Richardson S. M. and Uhle M. E. (2003) *Geochemistry: Pathways and Processes*. 2nd ed., Columbia University Press.

Mills B. J. W., Krause A. J., Jarvis I. and Cramer B. D. (2023) Evolution of Atmospheric O_2 Through the Phanerozoic, Revisited. *Annu. Rev. Earth Planet Sci.* **51**, 253–276.

Mißbach H., Duda J.-P., van den Kerkhof A. M., Lüders V., Pack A., Reitner J. and Thiel V. (2021) Ingredients for microbial life preserved in 3.5 billion-year-old fluid inclusions. *Nat. Commun.* **12**, 1101.

Mullin J. W. (2001) *Crystallization*., Elsevier Science & Technology, Chantilly, United Kingdom.

Norman D. I., Blamey N. J. F. (2001) Quantitative analysis of fluid inclusion volatiles by a quadrupole mass spectrometer system. *ECROFI* **7**, 341-344.

Ohno H., Iizuka Y. and Fujita S. (2021) Pure rotational Raman spectroscopy applied to N_2/O_2 analysis of air bubbles in polar firn. *J. Glaciol.* **67**, 903–908.

Onda K., Sada E., Kobayashi T., Kito S. and Ito K. (1970) Salting-out parameters of gas solubility in aqueous salt solutions. *J. Chem. Eng. Japan* **3**, 18–24.

Park J. G. and Schaller M. F. (2025) Constraints on Earth's atmospheric evolution from a gas-aqueous partition of fluid inclusion volatiles. *Gondwana Res.* **139**, 204–215.

Petit J. R., Jouzel J., Raynaud D., Barkov N. I., Barnola J.-M., Basile I., Bender M., Chappellaz J., Davis M., Delaygue G., Delmotte M., Kotlyakov V. M., Legrand M., Lipenkov V. Y., Lorius C., PÉpin L., Ritz C., Saltzman E. and Stievenard M. (1999) Climate and atmospheric history of the past 420,000 years from the Vostok ice core, Antarctica. *Nature* **399**, 429–436.

Pettitt E. A., Cherniak D. J., Schaller M. F. and Watson E. B. (2020) Diffusive retention of carbon and nitrogen in a microcrystalline quartz-dominated chert: Implications for reconstructing Earth's ancient atmosphere. *Chem. Geol.* **541**, 119572.

Pettitt E. A. and Schaller M. F. (2020) A new calibration technique for quantitative gas analyses of fluid inclusions using a quadrupole mass spectrometer. *RCM* **34**.

Pretet C., Reynaud S., Ferrier-Pagès C., Gattuso J.-P., Kamber B. S. and Samankassou E. (2014) Effect of salinity on the skeletal chemistry of cultured scleractinian zooxanthellate corals: Cd/Ca ratio as a potential proxy for salinity reconstruction. *Coral Reefs* **33**, 169–180.

Royer D. L. (2014) Atmospheric CO_2 and O_2 During the Phanerozoic: Tools, patterns, and impacts. In *Treatise on Geochemistry* Elsevier. pp. 251–267.

Schaller M. F., Wright J. D. and Kent D. V. (2015) A 30 Myr record of Late Triassic atmospheric pCO_2 variation reflects a fundamental control of the carbon cycle by changes in continental weathering. *Geol. Soc. Am. Bull.* **127**, 661–671.

Schaller M. F., Wright J. D. and Kent D. V. (2011) Atmospheric pCO_2 perturbations associated with the Central Atlantic Magmatic Province. *Science* **331**, 1404–1409.

Schreder-Gomes S. I., Benison K. C. and Bernau J. A. (2022) 830-million-year-old microorganisms in primary fluid inclusions in halite. *Geol.* **50**, 918–922.

Severinghaus J. P. and Battle M. O. (2006) Fractionation of gases in polar ice during bubble close-off: New constraints from firn air Ne, Kr and Xe observations. *EPSL* **244**, 474–500.

Steadman J. A., Large R. R., Blamey N. J., Mukherjee I., Corkrey R., Danyushevsky L. V., Maslennikov V., Hollings P., Garven G., Brand U. and Lécuyer C. (2020) Evidence for elevated and variable atmospheric oxygen in the Precambrian. *Precambrian Res.* **343**, 105722.

Sun Q., Zhao L., Li N. and Liu J. (2010) Raman spectroscopic study for the determination of Cl^- concentration (molarity scale) in aqueous solutions: Application to fluid inclusions. *Chem. Geol.* **272**, 55–61.

The Cenozoic CO_2 Proxy Integration Project (CenCO2PIP) Consortium*†, Hönisch B., Royer D. L., Breecker D. O., et al. (2023) Toward a Cenozoic history of atmospheric CO_2. *Science* **382**, eadi5177.

Tierney J. E., Poulsen C. J., Montañez I. P., et al. (2020) Past climates inform our future. *Science* **370**, eaay3701.

Van Eldik R. and Palmer D. A. (1982) Effects of pressure on the kinetics of the dehydration of carbonic acid and the hydrolysis of CO_2 in aqueous solution. *J. Solution Chem.* **11**, 339–346.

833 Vreeland R. H., Rosenzweig W. D. and Powers D. W. (2000) Isolation of a 250-million-year-old
834   halotolerant bacterium from a primary salt crystal. *Nature* **407**, 897–900.

835 Williams A. E. (1996) Mass spectrometric analysis of volatiles in fluid inclusions: aliquot
836   calibration valve to simulate inclusion rupture. *Chem. Geol.* **131**, 155–165.

837 Yan Y., Bender M. L., Brook E. J., Clifford H. M., Kemeny P. C., Kurbatov A. V., Mackay S.,
838   Mayewski P. A., Ng J., Severinghaus J. P. and Higgins J. A. (2019) Two-million-year-old
839   snapshots of atmospheric gases from Antarctic ice. *Nature* **574**, 663–666.

840 Yeung L. Y. (2017) Low oxygen and argon in the Neoproterozoic atmosphere at 815 Ma. *EPSL*
841   **480**, 66–74.

842 Zeebe R. E. and Wolf-Gladrow D. (2001) *CO$_2$ in Seawater: Equilibrium, Kinetics, Isotopes.*,
843   Gulf Professional Publishing.

844 Zimmermann J. L. and Moretto R. (1996) Release of water and gases from halite crystals. *Eur. J.*
845 *Mineral.* **8**, 413–422.

846

847

848

849

850

851

852

853

854

855

856

857

858

859

860

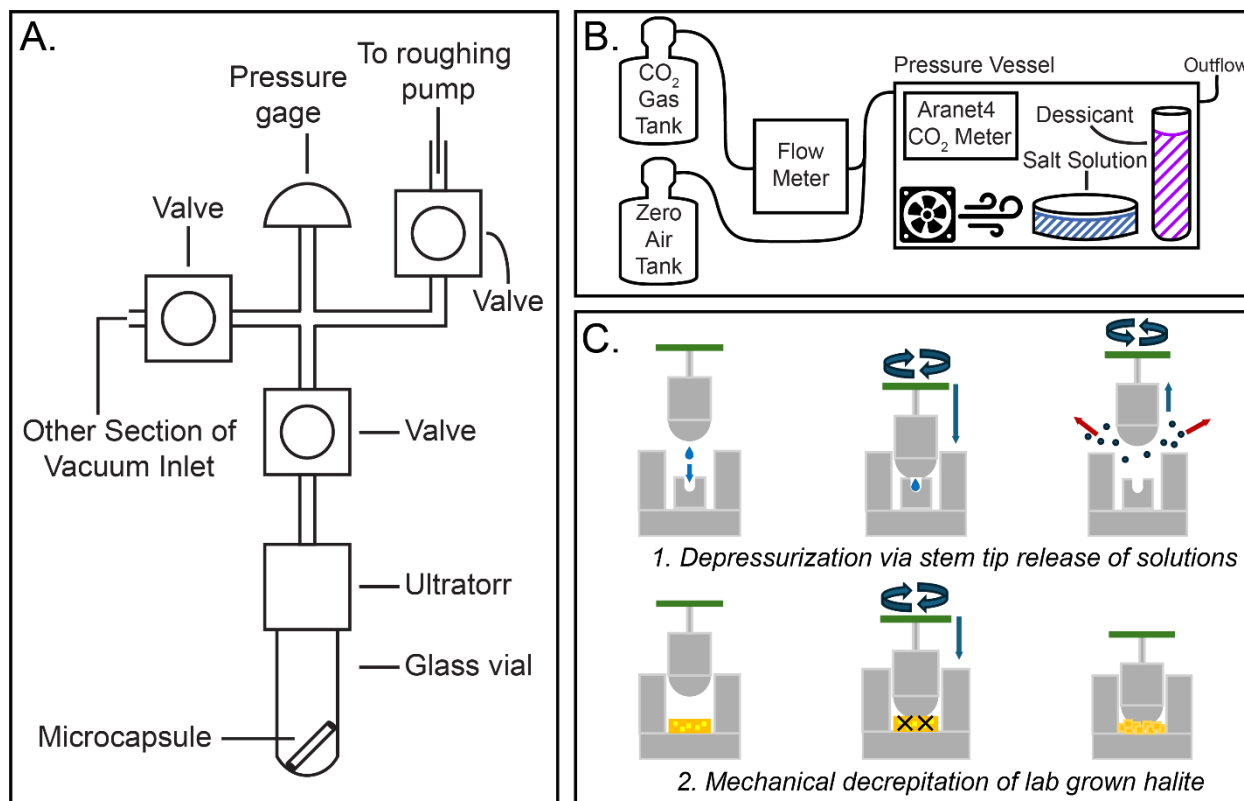861

862

863

864

865

866

867

Figures and Tables

Figure 1. Experimental procedure in this study. (A) Low vacuum (10^{-3} mbar) depressurization experiment setup for the 25 and 2 μL of 0.25 M $NaHCO_3$. Video for the low-vacuum depressurization experiment is linked to the "data availability" section of the online version. Note the decrepitation time is rapid (~5 ms). (B) Experimental pressure vessel setup for growing halite in an elevated pCO_2 environment. The vessel was held at 1 atm. (C) Schematic of stock solution depressurization and lab-grown halite decrepitation experimental procedure conducted under high vacuum on the quadrupole MS inlet line. (C.1) Volatiles were quantified via a stem tip release of the stock solutions (see Pettit and Schaller, 2020). (C.2) Volatiles in the inclusions of the lab-grown halite were quantified via mechanical decrepitation, releasing the entrapped volatiles from the inclusions.

883
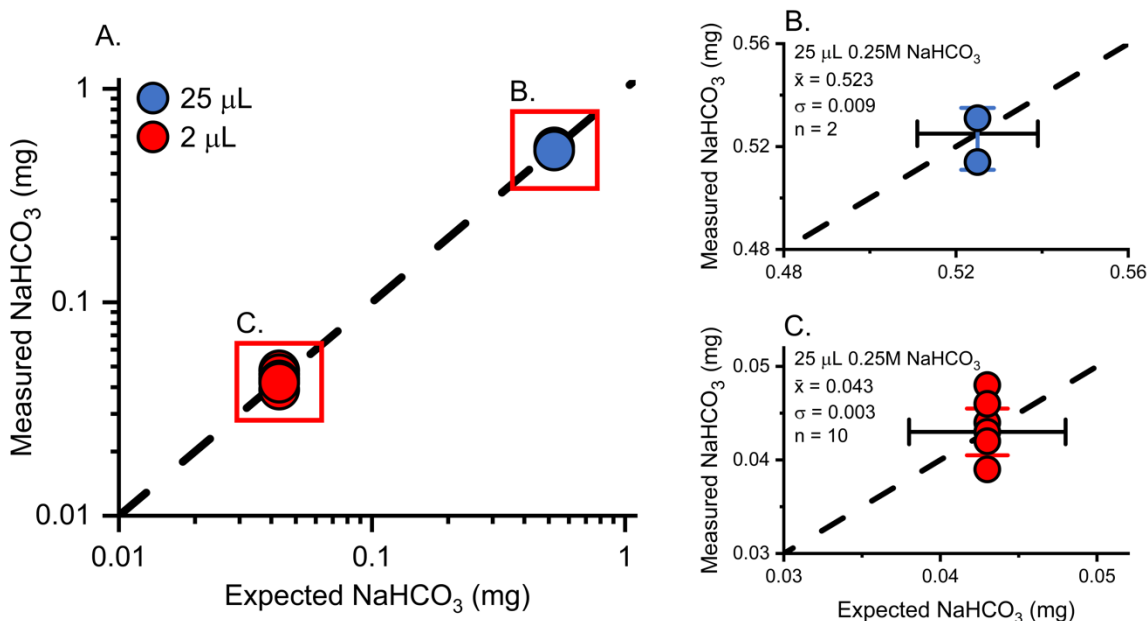
Figure 2. Mass of the expected residual NaHCO$_3$ (mg) vs mass of the measured residual
NaHCO$_3$ (mg) from the low-vacuum depressurization experiments on the 0.25 M NaHCO$_3$
solution at 25 μL and 2 μL volumes (A). Dotted line is the 1:1 for the expected vs measured
mass of the NaHCO$_3$ residue. Red boxes are the expanded areas for 25 μL (B) and 2 μL (C). X-
axis error bars are the syringe procedural volume error and colored y-axis error bars (blue and
red) are the standard deviation of the measured samples.

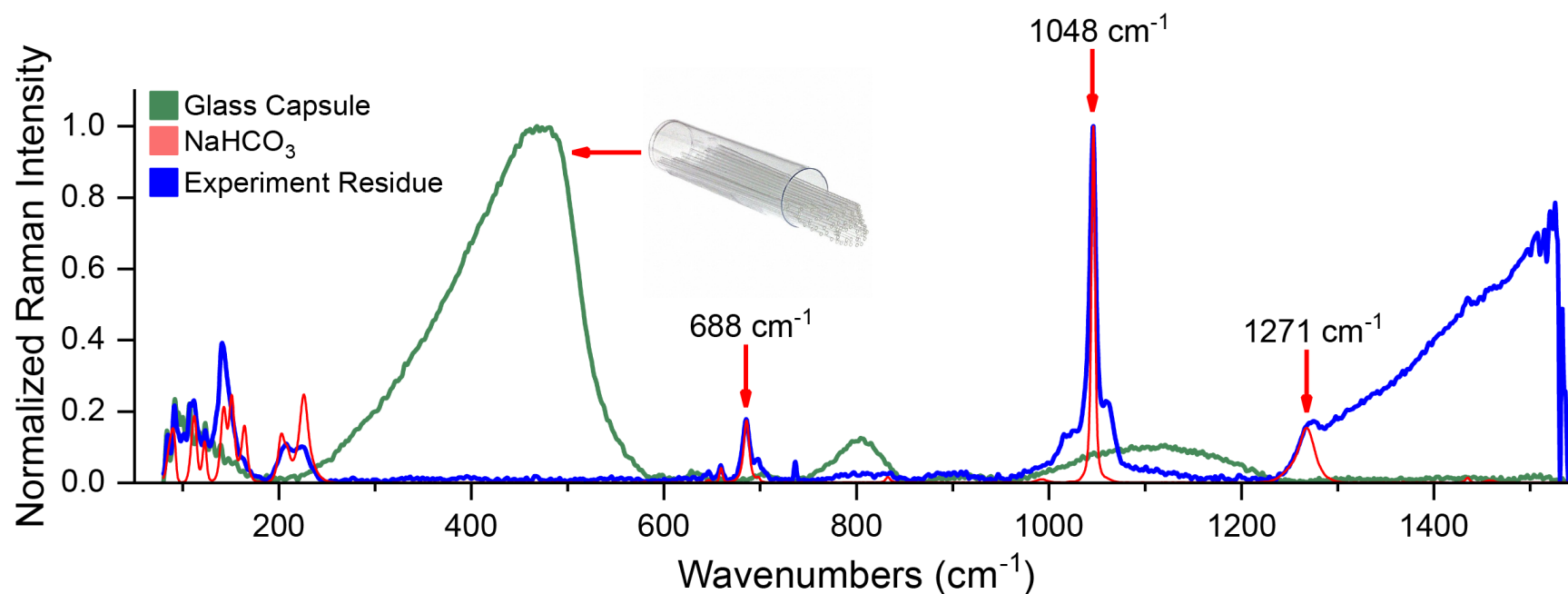**Figure 3.** Raman spectra of the residue from the low-vacuum depressurization experiments. The main bands for the $NaHCO_3$ salt are at 688, 1048, and 1271 cm^{-1} (pink). The spectrum of the experimental residue spectra (blue) are similar to the spectrum of the original $NaHCO_3$ salt, confirming the experiment residue is the original carbonate salt and is distinctly different from the spectrum of the glass microcapsule (green).
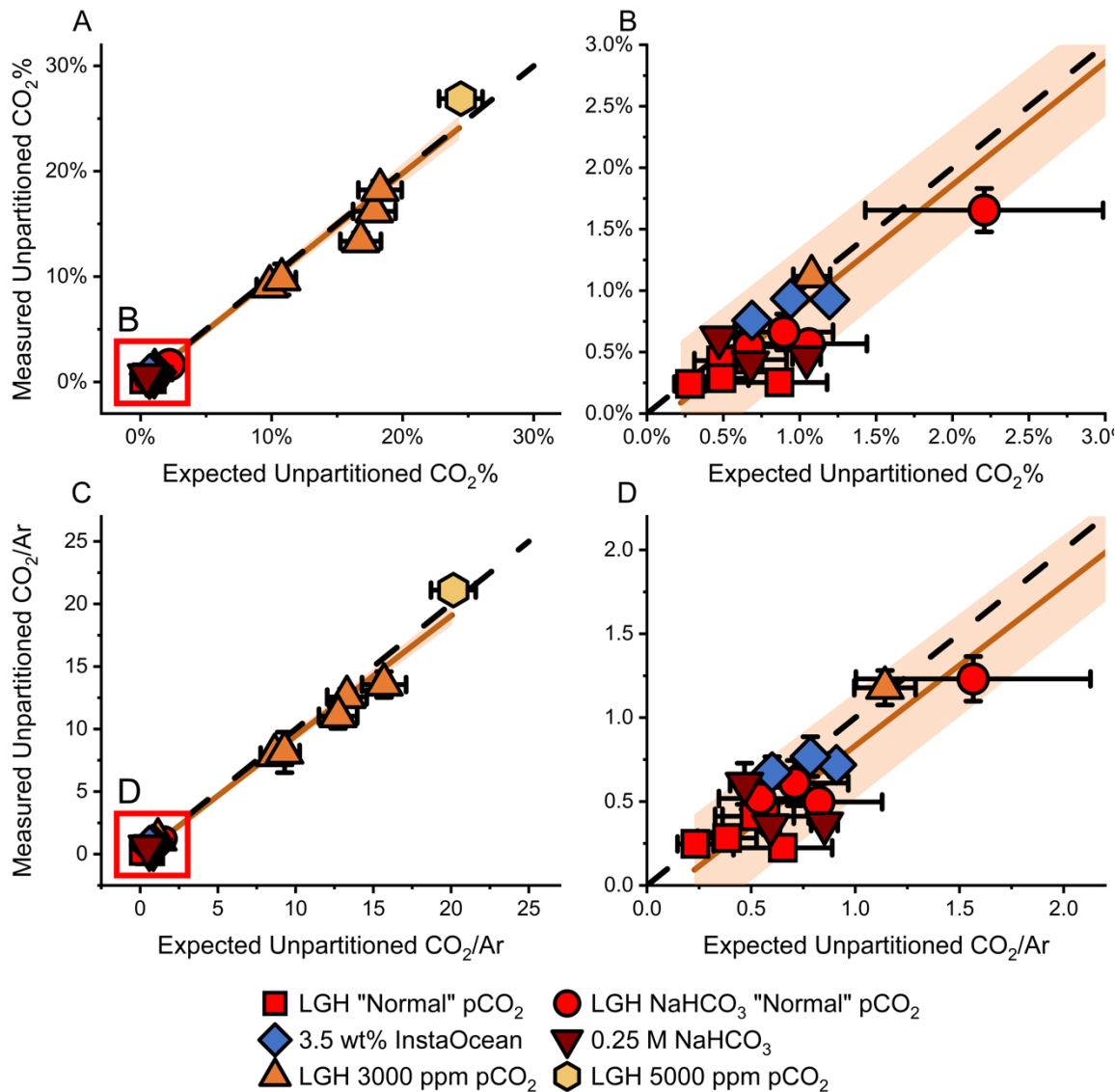
Figure 4. Results from the QMS measurements of depressurization and decrepitation experiments on the lab-grown halite (LGH) and the stock solutions. Expected vs measured CO_2 mol% (A-B) and normalized to argon (C-D) before partitioning between the aqueous and gaseous contributions. Red boxes are the expanded areas of the measured unpartitioned CO_2 mol% (B) and argon normalized CO_2 (D). Dashed line is the 1:1 of an air and air-saturated brine CO_2 mix, and the solid brown line is the linear relationship between measured and expected. Color-shaded areas are 95% confidence intervals. The error bars on the expected CO_2 were estimated based on the gas volume fraction and the range of CO_2 that the stock solutions and LGH were equilibrated under. The error bars on the measured CO_2 content are propagated uncertainties at the 95% confidence interval.
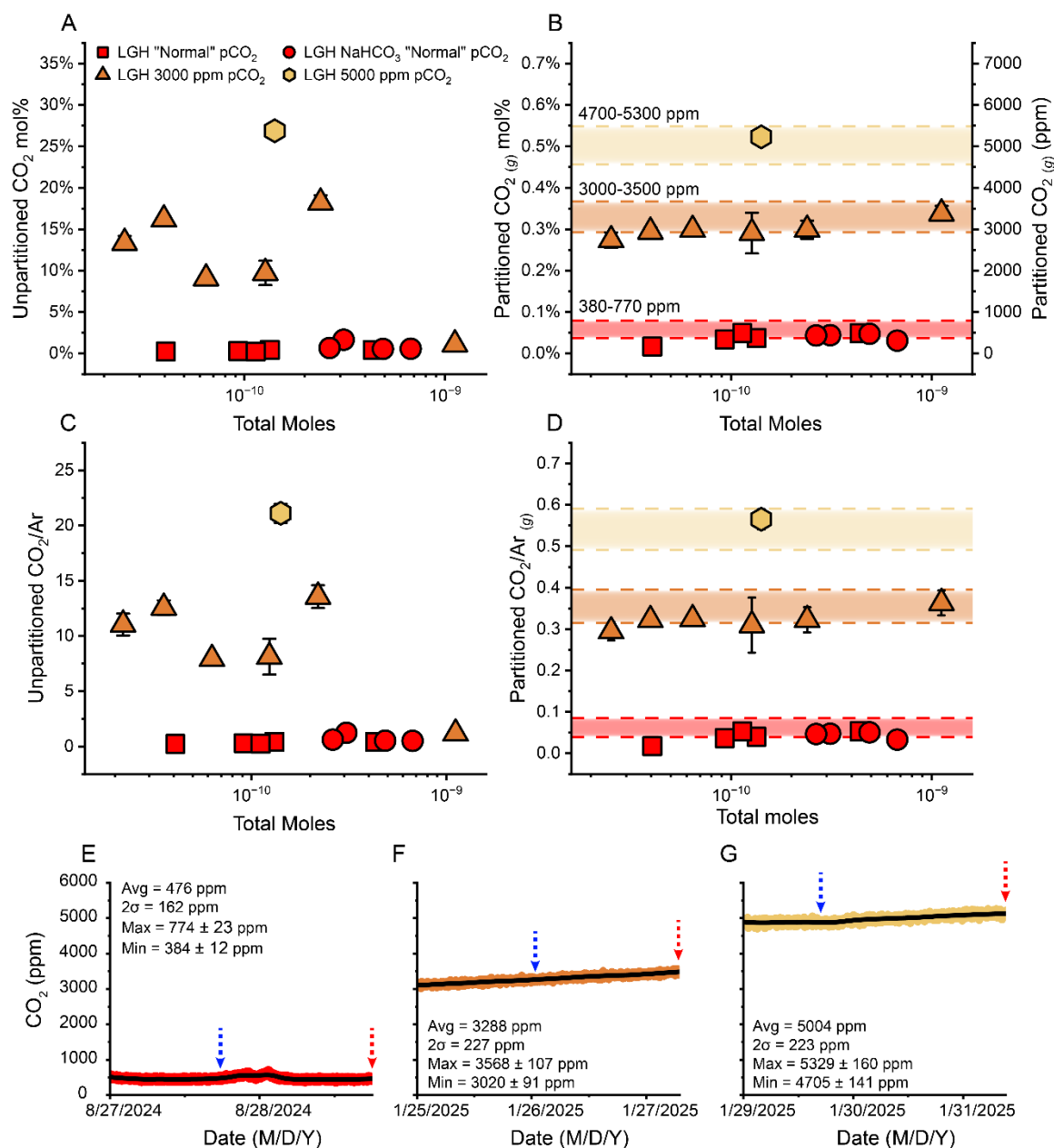
Figure 5. Total moles of measured gas (e.g., the sum of N_2, O_2, Ar, CO_2) versus the unpartitioned (A, C) and partitioned (B, D) CO_2 mol% and argon normalized CO_2 results from measurements of the lab-grown halite (LGH) decrepitation experiments. MAGPI was used to partition the raw inclusion data (Park and Schaller, 2025). Gas partitioned CO_2 measurements are compared to the monitored pCO_2 levels. LGH precipitated under "normal" (red, E) and elevated to 3000 ppm, (orange, F) and 5000 ppm (yellow, G) conditions. Blue vertical arrows represent the time points when hopper crystals were first observed during halite precipitation and red vertical arrows represent the time points when halite crystals were collected. Note that the LGH tracks the CO_2 concentration of the atmosphere with which the solutions were equilibrated and that partitioning of inclusion data is necessary for accurate interpretations. The error bars are propagated uncertainties.
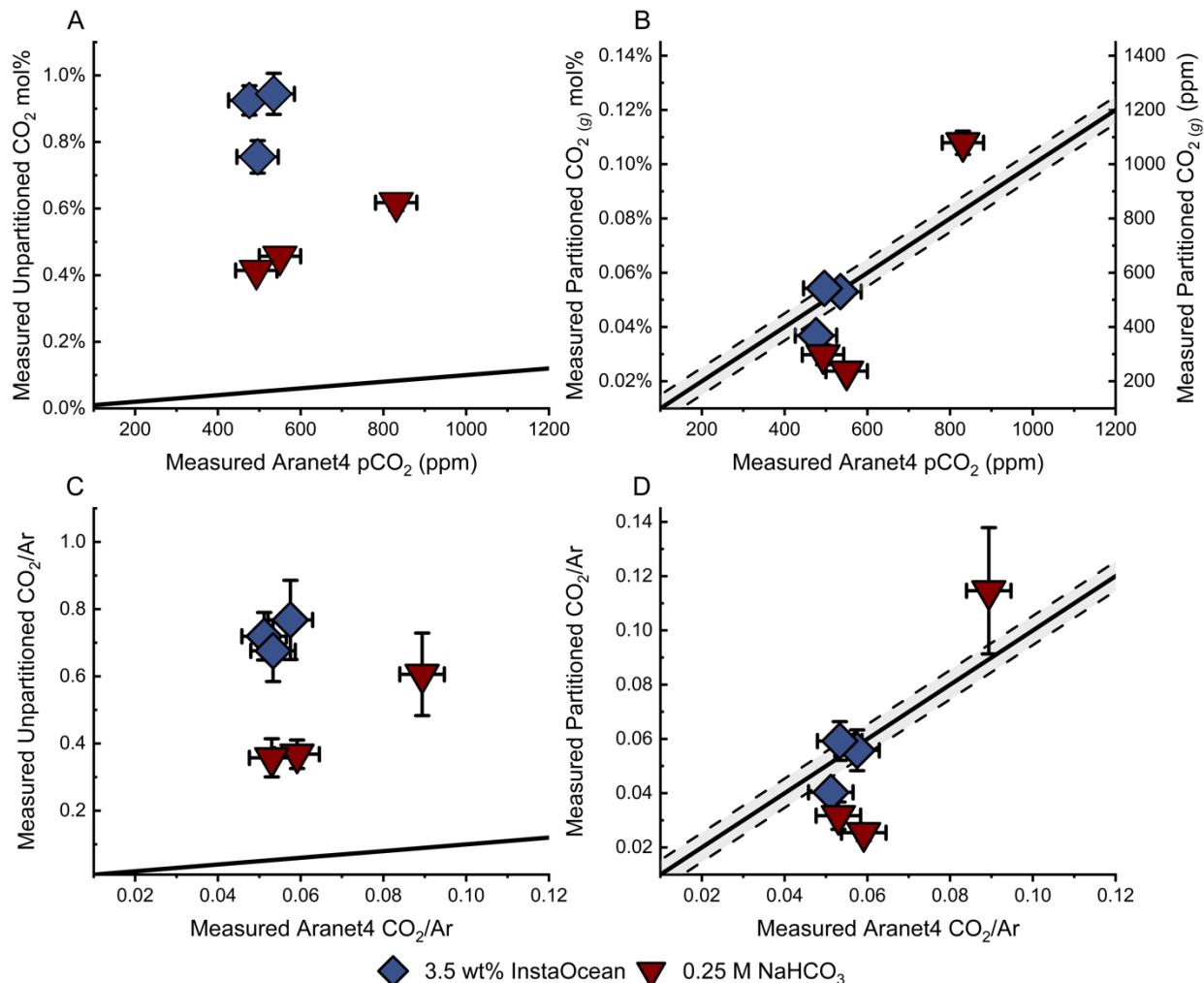
26

Figure 6. Measured pCO_2 (ppm) under which the solutions equilibrated vs. the unpartitioned (A, C) and partitioned (B, D) CO_2 mol% or CO_2/Ar from the solution depressurization experiments. The pCO_2 was measured by the Aranet4 CO_2 meter before the setup of each stock solution depressurization experiment. The argon to which the CO_2 was normalized was assumed to be at 0.93% in the laboratory. The solid black line is the 1:1 between the Aranet4 measured CO_2 and the QMS measured CO_2 mol% and CO_2/Ar. Dashed lines and grey shaded area are the error associated with the uncertainty in the Aranet4 CO_2 measurements at this range ($\pm$ 3%). The unpartitioned CO_2 noticeably diverges from the 1:1 line. However, the data partitioned using MAGPI (Park and Schaller, 2025) closely aligns with the 1:1 line. X-axis error is the CO_2 error of the Aranet4 and the y-axis error are propagated uncertainties.
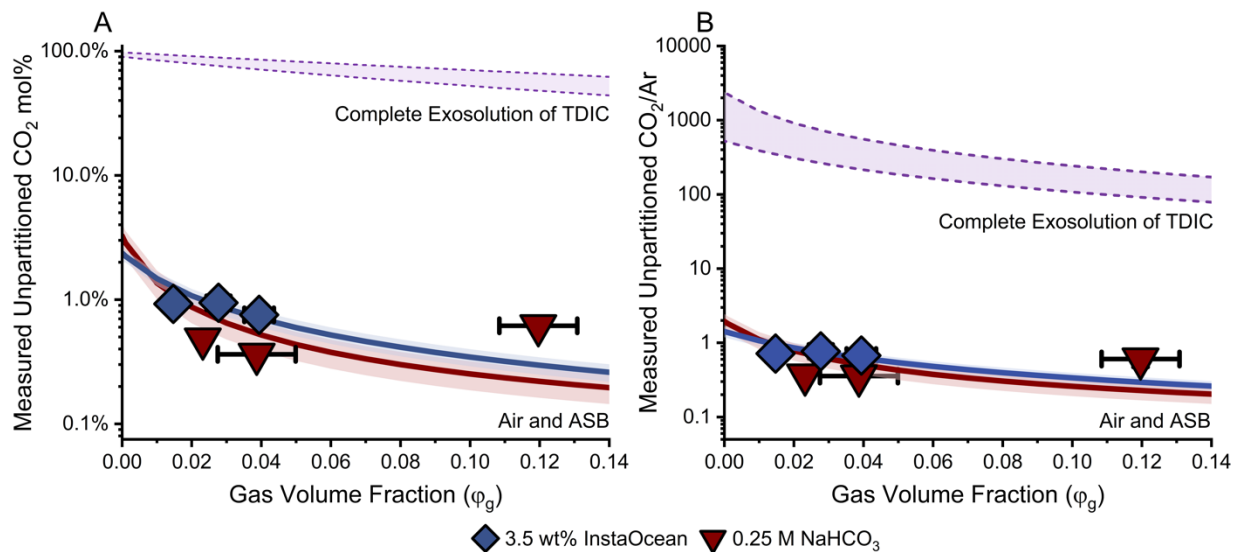
27

Figure 7. Results from the depressurization experiments. Measured gas volume fraction vs unpartitioned CO_2 mol% (log scale) (A) and argon normalized (B) on the 3.5 wt% InstaOcean (diamonds) and 0.25 M $NaHCO_3$ (inverted triangles) solutions. Solid blue and burgundy lines are the modeled expected values if the measured CO_2 represents a mix between air and air-saturated brine (ASB) for a NaCl and $NaHCO_3$ dominated solutions, respectively. Shaded blue and burgundy areas are the associated error for each air and ASB model. The upper and lower dotted purple lines are the model values where the measured CO_2 represents the complete exsolution of total dissolved inorganic carbon (TDIC) for a NaCl and $NaHCO_3$ dominated solution, respectively. The measured CO_2 content aligns with the expected for an air-ASB mixture. Note the prominent difference between the modeled complete exsolution of TDIC and the actual measured CO_2. X- and Y-axis error bars are the propagated uncertainty for the gas volume fraction and the measured CO_2, respectively.
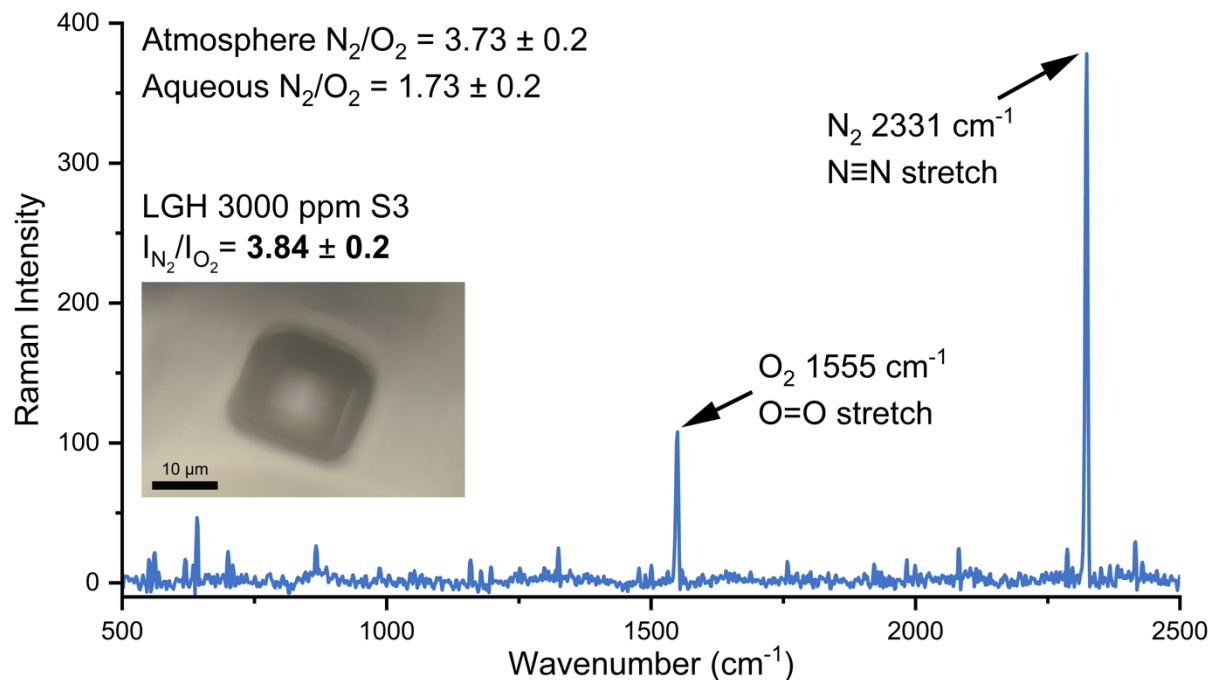
28

Figure 8. Raman spectrum of a fluid inclusion gas bubble in the lab-grown halite (LHG) that precipitated in 'zero air' (nominal atmospheric ratio of N_2, O_2 and Ar) with a maximum pCO_2 level of 3568 ± 107 and minimum pCO_2 of 3020 ± 91 ppm. The main N_2 and O_2 peaks are present at 2331 and 1555 cm^{-1}, respectively. The ratio between the intensities of the N_2 and O_2 peaks (3.84 ± 0.2) closely matches the gaseous N_2/O_2 endmember (3.73 ± 0.2) under which the LGH precipitated and does not overlap with the aqueous N_2/O_2 endmember (1.73 ± 0.2).
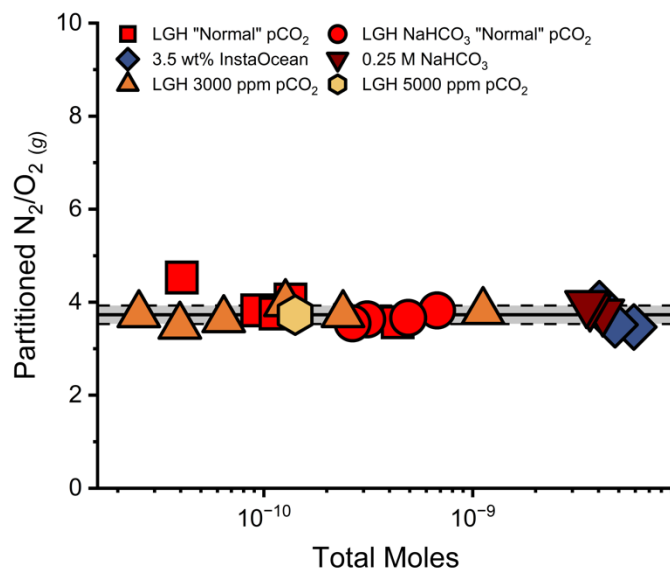
Figure 9. Partitioned $N_{2\,(g)}$ normalized to $O_{2\,(g)}$ results from the stock solution depressurization and the lab-grown halite (LGH) decrepitation experiments vs. total moles (sum of the measured N_2, O_2, Ar, and CO_2). Partitioned N_2/O_2 ratio of measurements is compared to the expected N_2/O_2 of the atmosphere under which the stock solutions and LGH equilibrated (solid black line). Dashed black lines and grey shaded area are the error range of N_2/O_2 for LGH precipitation. Stock solutions were equilibrated in open laboratory air and assumed N_2 was 78.08% and O_2 was 20.95%. Note that data converges to the atmospheric N_2/O_2 value (3.73 ± 0.2). Error bars are the propagated uncertainties.
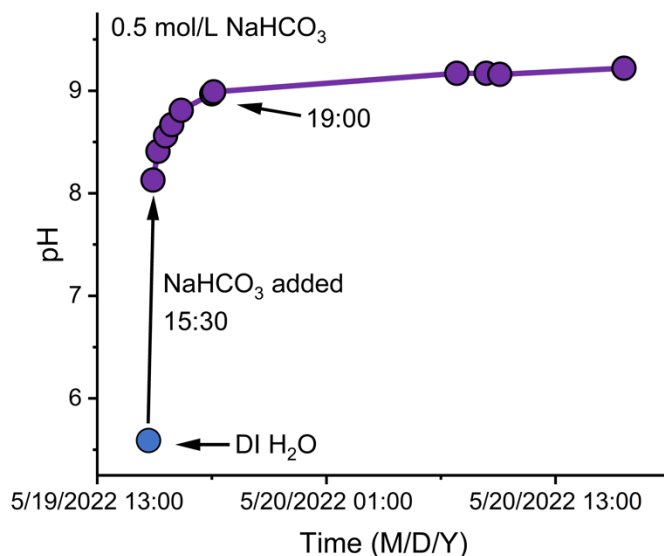

Figure 10. A 0.5 M $NaHCO_3$ solution was prepared to determine the time for atmospheric equilibration based on pH measurements. Prior to the addition of $NaHCO_3$ (blue), the pH of DI H_2O was ~5.5. When $NaHCO_3$ was added (purple), the solution reached pH equilibrium with the atmosphere after ~3.5 hours. Time is recorded in the 24-hour format with the time in month/days/years.

994

995
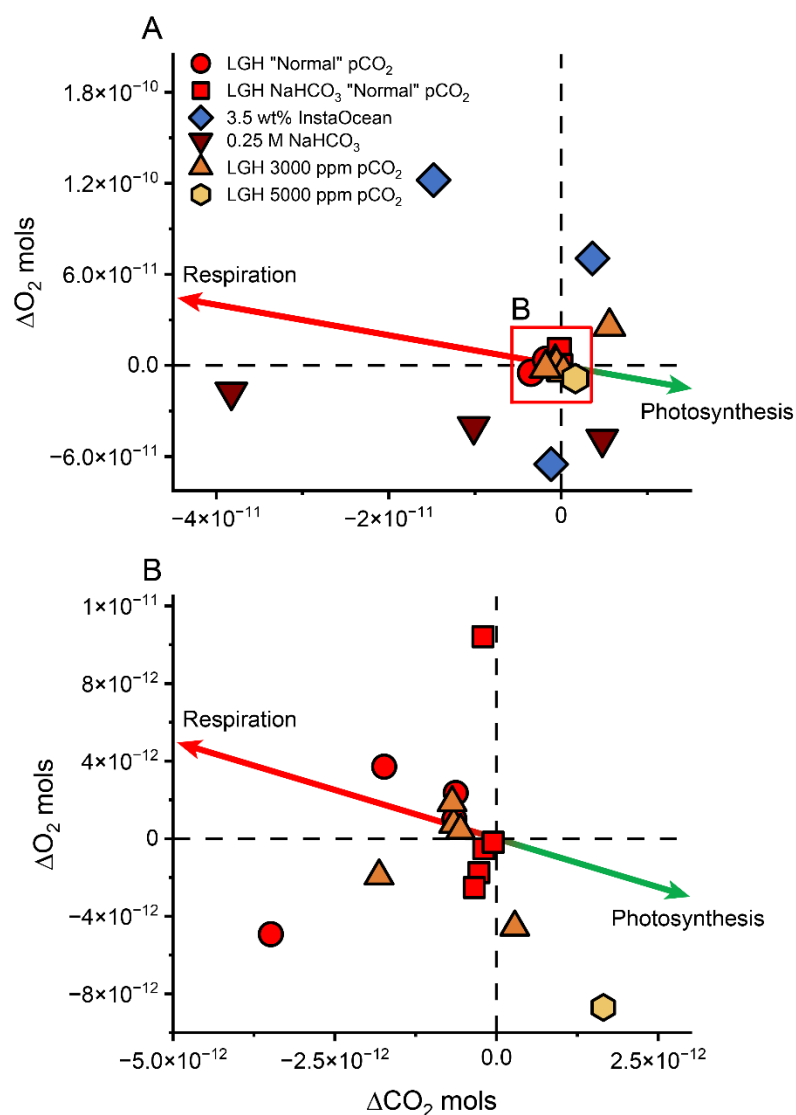
Figure 11. (A) Difference between measured and expected moles of CO_2 and O_2 in the stock solutions and lab-grown halite (LGH). Delta values are calculated relative to the samples respective atmospheric ratio using equation (6). (B) The expanded area of the red box in A. Green and red lines are the 1:1 expectation for stoichiometric exchange by photosynthesis and respiration, respectively. Black dashed lines represent the origin.

996
997
998
999
1000
1001
1002
1003
1004
1005
1006

1007 **Table 1.** Forward and reverse kinetic reaction rate constants for Eq. 1a-f

Reaction	Reaction direction	magnitude	Reference
Eq. 1a	k_{+1}	1.6×10^{-5} s^{-1}	calculated
	k_{-1}	4.1×10^{-4} s^{-1}	Choi et al. (1998)
Eq. 1b	k_{+2}	1×10^{4} $M^{-1} \cdot s^{-1}$	Eigen et al. (1961)
	k_{-2}	18.3 s^{-1}	Eldik and Palmer (1982)
Eq. 1c	k_{+3}	Instantaneously	Kern (1960)
	k_{-3}	Instantaneously	Kern (1960)
Eq. 1d	k_{+4}	59.4 s^{-1}	Zeebe and Wolf-Gladrow (2001)
	k_{-4}	5×10^{10} $M^{-1} \cdot s^{-1}$	Eigen et al. (1961)
Eq. 1e	k_{+5}	0.037 s^{-1}	Johnson (1982)
	k_{-5}	2.66×10^{4} $M^{-1} \cdot s^{-1}$	Zeebe and Wolf-Gladrow (2001)
Eq. 1f	k_{+6}	4.05×10^{3} $M^{-1} \cdot s^{-1}$	Johnson (1982)
	k_{-6}	1.76×10^{-4} s^{-1}	Zeebe and Wolf-Gladrow (2001)

1008

1009 **Table 2.** Measured mass of the residue from the low-vacuum depressurization experiments
1010 compared to the residue mass expected from the syringe on the 0.25 M $NaHCO_3$ solutions at 2
1011 and 25uL.

0.25M $NaHCO_3$	Measured Residue (mg)	Syringe Procedural Range (mg)
2 μL (n=10)	0.043 ± 0.003	0.043 ± 0.003
25 μL (n=2)	0.523 ± 0.009	0.525 ± 0.014

1012

1013 **Table 3**. Correlations between the measured vs. expected unpartitioned CO_2 mol% and CO_2/Ar,
1014 and ANOVA and ANCOVA results with F-test and associated p-value of the measured
1015 unpartitioned CO_2 mol% and CO_2/Ar compared to the 1:1. Bolded values are significant.

	Equation	R^2	ANOVA		ANCOVA	
			F	$p(\alpha)$	F	$p(\alpha)$
Unpartitioned CO_2 mol%	y=0.99x-0.003	0.98	0.025	0.88	2.77	0.10
Unpartitioned CO_2/Ar	y=0.96x-0.18	0.99	0.038	0.85	6.56	**0.01**

1016

1017

1018

1019

1020

1021

1022

1023

Table 4. Comparisons between the average and standard deviation of the CO_2 content before and after applying the gas-aqueous partition to lab-grown halite (LGH). Partitioned compositions closely match the compositions under which the LGH equilibrated.

Samples	CO_2 mol%	CO_2/Ar
LGH "Normal" pCO_2 (n=5)		
Unpartitioned	0.3305 ± 0.0973	0.3156 ± 0.0906
Partitioned	0.0374 ± 0.0134	0.0400 ± 0.0148
LGH $NaHCO_3$ "Normal" pCO_2 (n=4)		
Unpartitioned	0.8574 ± 0.5338	0.7140 ± 0.3480
Partitioned	0.0410 ± 0.0070	0.0443 ± 0.0078
LGH ~3000 ppm pCO_2 (n=6)		
Unpartitioned	11.2851 ± 6.1200	9.0663 ± 4.4880
Partitioned	0.2992 ± 0.0212	0.3227 ± 0.0227
LGH ~5000 ppm pCO_2 (n=1)		
Unpartitioned	26.8913	21.1087
Partitioned	0.5230	0.5652
Aranet4 CO_2	**Minimum**	**Maximum**
LGH "Normal" pCO_2	0.0384 ± 0.0012	0.0774 ± 0.0023
LGH ~3000 ppm pCO_2	0.3020 ± 0.0091	0.3568 ± 0.0107
LGH ~5000 ppm pCO_2	0.4705 ± 0.0141	0.5329 ± 0.0160

Table 5. Comparisons between the average and standard deviation of the CO_2 content of stock solutions both before and after applying the gas-aqueous partition. Partitioned compositions closely match the compositions in which the stock solutions equilibrated under.

Samples	CO_2 mol%	CO_2/Ar
3.5 wt% InstaOcean (n=3)		
Unpartitioned	0.8729 ± 0.0999	0.7211 ± 0.0460
Partitioned	0.0480 ± 0.0096	0.0518 ± 0.0101
0.25 M $NaHCO_3$ (n=3)		
Unpartitioned	0.4963 ± 0.1074	0.4439 ± 0.1405
Partitioned	0.0538 ± 0.0470	0.0573 ± 0.0498